Towards pronking with a hexapod robot

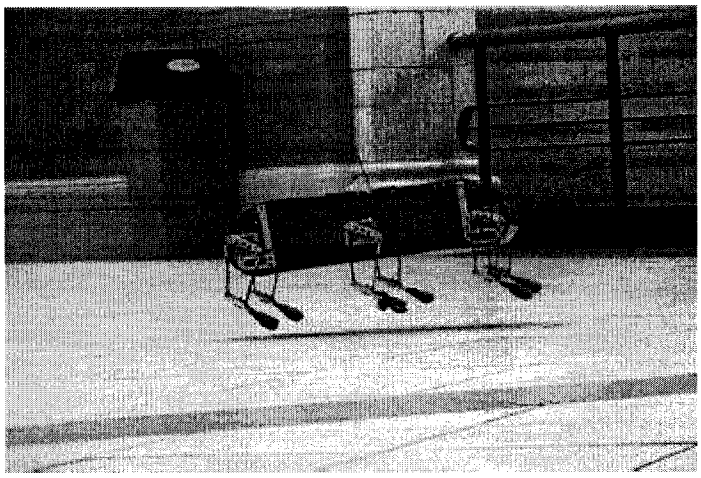

Dave McMordie
Department of Electrical Engineering
McGill University, Montreal, Canada
July, 2002

A thesis submitted to the Faculty of Graduate Studies and Research in partial fulfillment of the requirements of the degree Master of Engineering

Your file Votre référence
ISBN: 0-612-85890-1
Our file Notre référence
ISBN: 0-612-85890-1

Abstract

RHex is a robotic hexapod with springy legs and just six actuated degrees of freedom. This work presents the development of a pronking gait for RHex, extending its efficiency and speed by exploiting its springy legs for hopping. A simple physical model of pronking is presented and verified qualitatively in simulation and experiment. In the course of analysing and attempting to stabilize pronking, the author develops an inertial attitude estimation system for RHex built around a three axis fibre-optic gyroscope. The author also validates a simple current estimation model for RHex's motors, which is then used to detect leg touchdown during pronking.

Résumé

RHex est un robot à six pattes dont chaque jambe élastique est contrôlée par un seul moteur, placé a la hanche. Cette thèse décrit le dévelopment d'une nouvelle démarche pour RHex, le « pronk ». Cette démarche a permit une améloration de vitesse et éfficacité de locomotion de RHex, à cause de l'utilisation des jambes élastiques pour controller la motion verticale du centre de masse. En essayant de comprendre et de contrôler le « pronk », l'auteur a construit un nouveau système d'estimation d'orientation basé sur un gyroscope fibre-optique à trois axes. L'auteur a aussi verifié un modèle simple pour l'éstimation du courant dans un moteur qui est utilisé pour détecté l'atterisage du robot.

Acknowledgements

Robotics research involves a huge amount of design, manufacturing, procurement and administration. Like all aspects of the RHex project, this work was successful as much because of the hard work of the other members of the RHex team as because of my own efforts. I would especially like to thank those individuals whose contributions, technical or otherwise were essential to the author's work:

- Martin Buehler (my advisor) for his guidance, ideas, criticism, support; for inventing RHex; and for fostering a strong sense of quality, team spirit and motivation in his lab.
- Uluç Saranli for endowing RHex with its first physical incarnation and two generations of control software
- Ben Brown and Edward Moore for designing the compliant four-bar legs used for pronking.
- Felix Grimminger for designing the half-circle legs which RHex has used over so much difficult terrain.
- Don Campbell for designing RHex's I/O system, as well as his numerous other technical and creative contributions
- Matt Smith for his inspired and beautiful design of all things mechanical on RHex
- Haldun Komsuoglu for collaborating on numerous aspects of electronic design, and for many animated RHex discussions
- Joel Weingarten showing us all how much further RHex can go with a little learning.
- Karen Coulter for her intrepid support of demos, software, hardware and administration for the RHex project.
- Dan Koditshek for putting together and leading the RHex project; for guidance and support throughout this project.

- Sarjoun Skaff for taking inertial sensing on RHex to a whole new level.
- Al Rizzi for help with the gyro interface thread, as well as many interesting discussions.
- Prof. Robert J. Full for making the series of discoveries about animals which motivated the construction and study of RHex; for many valuable discussions.
- Prof. Peter Caines for going the extra mile in helping me understand Kalman and Wiener filtering and how Kalman filtering may be applied to attitude estimation.
- Team Northern Sun, McGill's Solar Vehicle Project for allowing me the opportunity to learn both team working and real-world design skills.
- Guy-Anne Turgeon, Martin Cloake for the construction of T-RHex, a low cost, scalable version of RHex.
- The four horsemen, Jean E. Collin, Grand Smedley, Mathieu Bernier, Thomas Lavertu for the design and assembly of the shell version of RHex.
- Danny Chouinard and Jan Binder for keeping CIM's computer facilities running, providing the tools and technologies we need to keep the lab going.
- Marlene Gray and Cynthia Davidson for keeping CIM operational and properly caffeinated.
- Genvieve Vinois for her invaluable administrative support, creativity and hard work in keeping the lab operational.
- Ioannis Poulakakis, James Smith, Evgeni Kiriy and Carl Steeves for inspiring discussions about other ARL robots, and for their ideas about RHex. Thanks also to James for helping me

translate the abstract, and for a careful reading of the Attitude Estimation chapter.

- My parents, Claire and Michael McMordie, for their love and support throughout this work, and for a close reading of several drafts.

Finally, I would like to thank Heather Butler for her love, patience and support throughout this programme. It seemed to me that every time I got stuck on a problem Heather was there with both good ideas and encouragement. Thanks also to Heather for a careful last reading of this thesis.

Contents

Figures

Tables

Chapter 1 Introduction, Background and Overview

1.1 Why we build legged machines

A key feature of many robots that are intended to perform useful work in the world is that they must be able to navigate unassisted both indoors and out. We therefore study legged locomotion in order to address the first, and perhaps most fundamental, need of robots which may one day be both power and task autonomous: mobility. Only robots that can locomote freely in real-world environments without human assistance are candidates for real-world tasks.

1.2 Wheeled and Tracked Robots

After many years of research and development wheeled and tracked robots are beginning to show their maturity in real world tasks. Wheels and tracks give rise to simple, stable robots with a great range of mobility. For this reason, they have been the only serious contenders for real-world autonomous robotic applications to date.

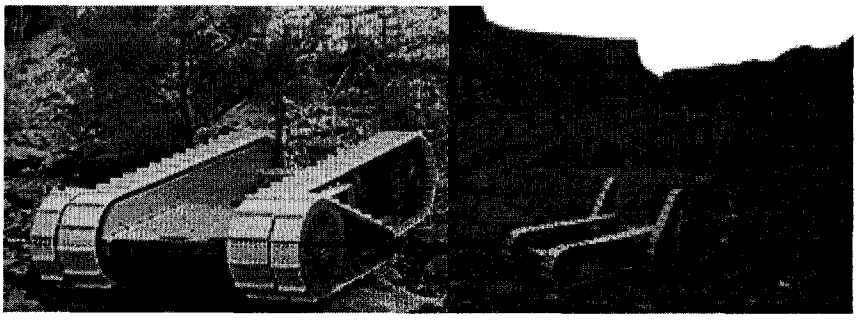

Figure 1a,b: Packbot: a state of the art tracked-robot

Figure 1 shows "Packbot" a recent version of the Urbie articulated tracked robot, designed by iRobot Corp.[1]. The Urbie series of robots has been one of the most successful in military and police applications, successfully performing demonstrations of rescue and surveillance applications for military and law-enforcement personnel.

While tracked and wheeled robots have demonstrated an impressive degree of mobility in unstructured environments, they still pale in comparison to animals in robustness, efficiency and agility. A key hope driving the study of legged locomotion is that legged robots may one day be capable of far better mobility than wheeled and tracked robots of similar size and weight.

1.3 History and Inspiration of RHex

Inspired by the findings of R. J. Full [2] in the study of cockroach locomotion over broken terrain, the first version of RHex was constructed in 1999 by M. Buehler and U. Saranli [3]. This followed a demonstration by M. Buehler of a simulation showing that cockroach-like locomotion might be achieved with just six motors and a simple CPG*-style control algorithm.

Full's findings suggest that in their fastest modes of locomotion, cockroaches appear to shun task-level, or indeed any extereoceptive, feedback in the control of their gait; they prefer to move their legs in a strictly open-loop fashion [4]. This observation was exploited in implementation of a simple and highly agile alternating tripod gait on RHex. The tripod gait is so named because at any one time at least

---

* Central Pattern Generator

three legs including the fore and aft leg from one side, and the middle leg from the other side, are in contact with the ground. During the stance phase of one tripod, the other tripod sweeps an arc from the back of stance (liftoff angle) to the front of the next stance (touchdown angle). With springy legs, this gait permits both statically stable operation (ie. if the robot were frozen in motion at any point, it would not fall over) and dynamic running (during running, legs act as springs, and the center of mass is at its lowest point close to mid-stance). Since its inception, the tripod gait has been the robot's primary mode of locomotion, moving it over obstacles previously negotiated by only the best wheeled and tracked platforms.

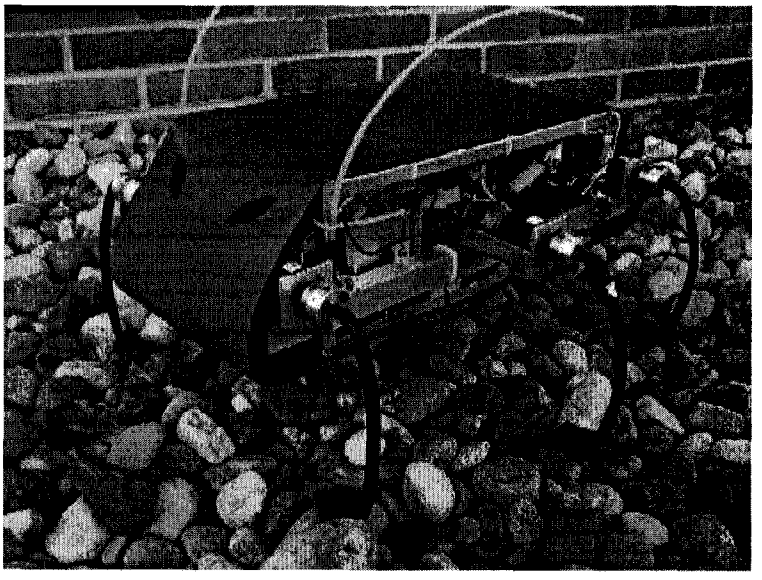

Figure 2: Rhex 0: First version of the robot built by U. Saranli and M. Buehler

While RHex's tripod gait was a powerful locomotion tool, it was initially limited in its speed and efficiency.

1.4 Motivation for running gaits

With a robust and effective tripod gait already in place, the author saw the need to attempt a higher-speed aerial-phase gait in order to more

efficiently and rapidly tackle the wealth of smooth terrain presented by certain urban contexts such as roads and floors. Although the more substantial reward in studying legged robotics would be to run at high speed over rough terrain, a more reasonable goal in the short term is to develop running behaviours that would consistently perform over smooth surfaces. It is hoped that such running behaviours will one day generalize to rougher terrains.

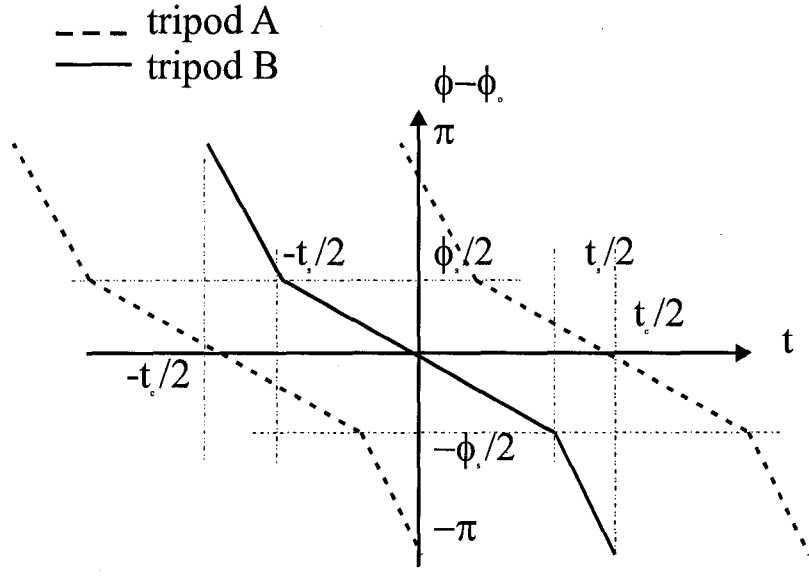

Figure 3: Desired leg angles versus time for RHex's tripod walk (based on figure from [3])

In RHex's statically stable tripod walk (ie. with overlapping tripod stances), forward speed is limited by the speed with which one can circulate each leg from the end of one stance phase to the beginning of another. This means the maximum speed of the robot will be dictated by the recirculation speed of the one tripod through a large (~300 degree) arc (approximately 200 ms, based on a no-load maximum leg speed of 5 rev/s). The tripod in stance sweeps simultaneously through the remaining 60 degrees in the same 200 ms, resulting in a maximum

walking speed of approximately 0.7 m/s (based on a leg length of 14 cm).

The energetics of walking may also be a limitation. During stance force must be applied to support the weight of the robot when the leg is not directly beneath its hip. Since the actuators on RHex dissipate power when they apply force (even if no work is done), the support of body mass equates with potentially large power losses.

Running gaits address both of these concerns. By exciting the leg springs the force needed to support the robot's weight and propel it into the air is supplied primarily by storage and release of energy in the leg springs. Energy input from actuators is required only to compensate for energy loss due to damping and for control of balance. Further, the retraction phase may now take place underneath the robot, minimising the arc travelled by the leg in flight, and hence the time between successive stance phases.

As it was unclear which running gaits would best suit a hexapod (aside from an obvious extension of the alternating tripod gait to an aerial-phase run*), pronking was selected as an obvious candidate to allow the transition of insights gained in the study legged running robots. As we shall see, pronking is a gait that can be described with simple model, and is capable of great speed and efficiency.

---

* Ongoing research at University of Michigan by Joel d. Weingarten and Prof. Daniel Koditschek has resulted in a stable open-loop alternating tripod run at up to 2.5 m/s.

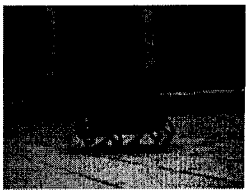

1.5 Pronking?

Pronking is a one-beat running gait in which the stance phases of all legs are coincident. Pronking is rarely used for running any distance, but llamas, deer, impalas and springboks all use pronking either during play, or when startled. Animal pronking gaits are characterized by very high ground clearance and low duty cycle, ie. much more time spent in the air than on the ground. It has been suggested [5] that this increased clearance may be useful both for seeing further, and for disseminating warning scents when predators are near.

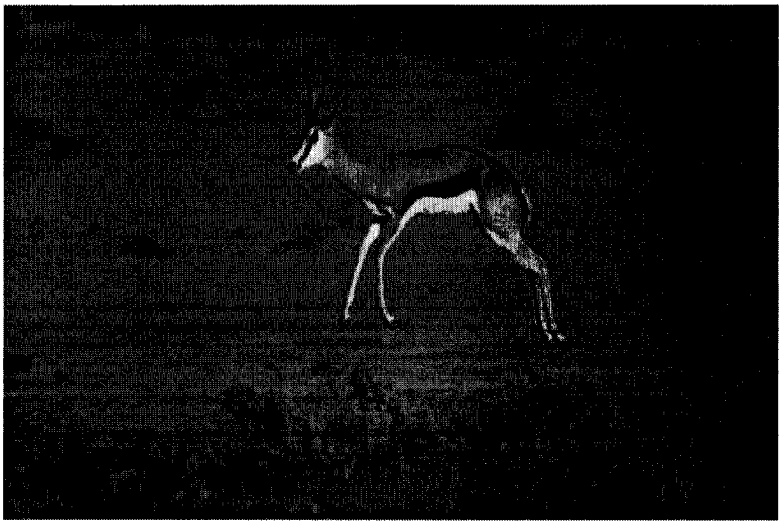

Figure 4: Springbok pronking*

Though pronking is neither a cockroach gait, nor indeed the gait of any hexapod creature of which the author is aware, the study of pronking is simply another effort to exploit concepts found in nature to improve the performance and expand the behavioural repertoire of robots. In this case, we recognise that the RHex's resilient leg springs and powerful hip

* This image was taken from a website which was no longer extant at time of printing.

actuators may make it suitable for more quadruped-like gaits such as pronking and bounding, in addition to the highly successful tripod walk.

Pronking, as opposed to bounding or trotting or other gaits was selected for three reasons. First, it was thought to exploit the same basic patterns of motion used by monopod hoppers, for which many useful results have already been obtained. Second, it uses all six legs in an obvious manner, as opposed to for instance bounding, where it is unclear what to do with the middle legs. Third, the author had reason to believe that control of pronking could be achieved with just the six actuators already installed on the robot—no lateral hip actuation or radial leg actuation appeared to be necessary.

Pronking is only one of three running gaits being developed for RHex. The alternating tripod run (similar to the tripod walk, but with an aerial phase and much greater speed) is the subject of ongoing research at University of Michigan by Joel d. Weingarten and Prof. Daniel Koditschek has resulted in a stable open-loop alternating tripod run at up to 2.5 m/s. Don Campbell and M. Buehler are also developing a bounding gait for RHex in which the middle legs are stowed to turn RHex into a quadruped.

Though pronking was primarily selected in order to study the more general class of dynamic running gaits, it may have some intrinsic advantages as well. It is likely that pronking can achieve higher ground clearances during flight than for instance bounding. This may one day be an advantage for obstacle traversal, especially when one considers the small size of RHex.

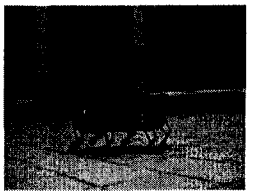

1.6 Relevant Work

Raibert [6, 7] and colleagues built simple running monopods, bipeds and quadrupeds in the 1980s and 90s which were capable of fantastic mobility and speed. Many of the simple insights into the dynamics of running used in this thesis have their roots in statements and equations written by Raibert and his team.

In particular, Raibert asserted three key points, which serve as a foundation for any study in legged locomotion. Firstly, stance and flight vertical dynamics may be viewed as coupled spring-mass and gravity mass oscillators, with the stance time fixed by the effective spring constant of the leg and the mass of the robot. Secondly, a symmetric stance phase serves as a sufficient condition for stability in running (and hence for every forward speed there exists at least one touch down toe placement that will result in stable hop) [8]. Thirdly, body pitch during stance may be stabilized by means of torques applied about the center-of-mass during stance.

Previous ARL Robots

Continuing in the tradition of Raibert, Ahmadi and Buehler built monopod runners ARL Monopod I and II [9]. With the insights gained into the role of springs in robot locomotion, Buehler *et al* built quadrupeds Scout I [10] and Scout II [11], developing with the latter robot insights into both bounding and pronking with springy legs. These four robots are shown in Figure 5.

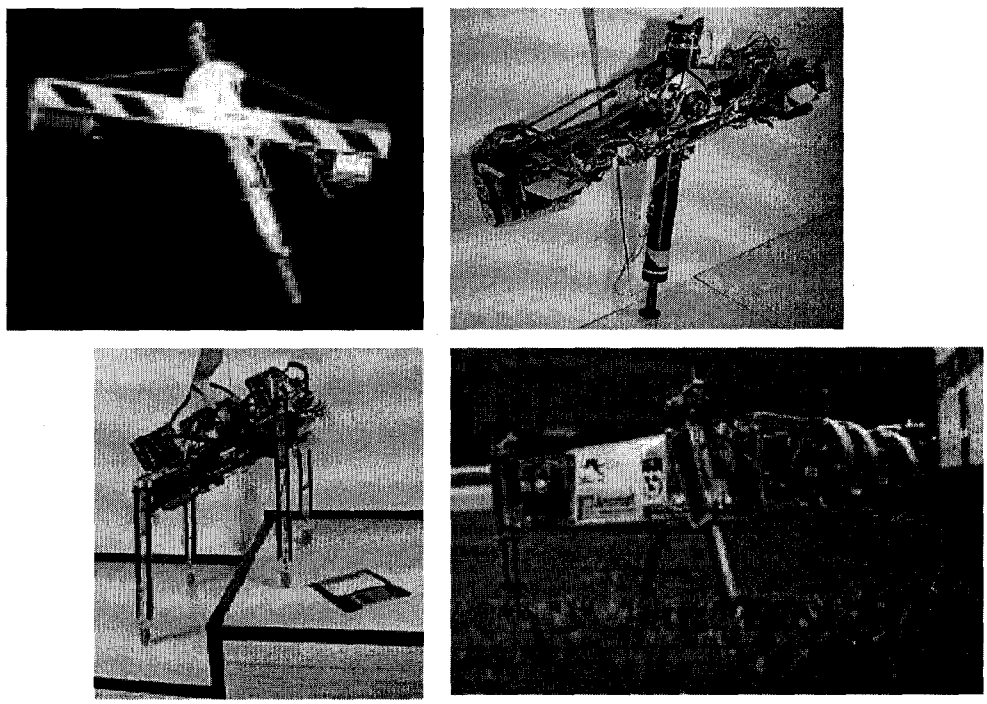

Figure 5: Robots previously constructed at ARL. Clockwise from top left: Monopod I, Monopod II, Scout I, Scout II

Though none of the previous ARL robots were hexapods, each of them contributed to concepts and discoveries strongly relevant to RHex, and specifically to the development of the pronking controller. The most significant of these developments were the following:

- Actuation at the hip of otherwise un-actuated legs can be used to generate stable and useful multi-legged gaits [10,11].
- Prismatic springy legs can be used to develop high-speed, high-efficiency gaits.
- Robot actuation and sensing fidelity may be a determining factor in gait behaviour.

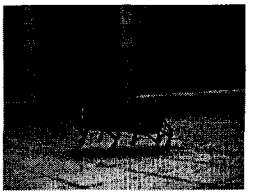

Other robots

Although numerous hexapod robots have been built to date, the most famous being Genghis [12], built by R. Brooks and others at the MIT AI lab, to the author's knowledge only Sprawlita [13] was capable of dynamic running. Similar to RHex, Sprawlita is inspired by biology, aiming to capture essential functional aspects of animal locomotion without attempting to copy all actuation and morphological details. It achieves a top speed of 42 cm/s or 2.5 body lengths per second. Since Sprawlita is powered by external pneumatics, it appears that RHex is the first and so far only power-autonomous hexapod capable of dynamic locomotion, and the only one capable of pronking.

Pronking has been modelled in quadrupeds [14], but the few quadrupedal running robots built to date use bounding or trotting gaits [15,16].

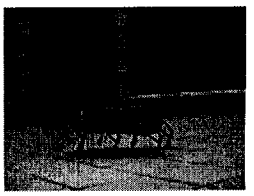

Chapter 2 Motor Modelling and Current Estimation

2.1 Background and Motivation

High performance control requires high performance sensing and actuation

At the heart of legged locomotion research is the control of high-complexity, often unstable or marginally stable, dynamical systems. To properly address the challenges imposed in this environment a combination of reliable sensing, accurate modeling and high fidelity actuation are required. This chapter addresses the last of these requirements: design, modeling and basic characterization of the motor and drive combination onboard RHex.

In legged locomotion, actuators not only add energy to the dynamical system, but also can have profound effects on the stability, behaviour and performance of gaits. In another ARL robot, Scout II, it was unclear for more than a year why one gait controller caused the robot to pronk in simulation and bound in experiment. When the batteries were upgraded to a higher performance pack during a redesign of the electronics, the robot began pronking in experiment. After some analysis it became evident that saturation of the current being drawn from the batteries was limiting actuator torque and may have been responsible for the difference in behaviour.

RHex, unlike other dynamic robots built at ARL has no direct means to measure motor current or leg torque. Leg torque is obviously a very important variable in the analysis and control of legged locomotion, so

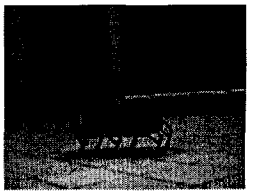

some trouble was taken to model the motor current (from which we infer leg torque) in each of RHex's motors. A preliminary model for motor current, along with experimental validation, is presented in the next section. This model is used in both the PD servo control of each of RHex's legs, but in a simple state machine which detects leg touchdown during pronking as well. Although future versions of RHex may incorporate current or torque sensing, we would prefer to continue to model current (if it can be done precisely) so as to keep the complexity of RHex's motor drive electronics to a minimum.

2.2 A Motor / Drive Model For Open Loop Torque Control

This section derives a simple model of the relationship between the duty cycle of a PWM amplifier (in this case the SA60 module [19]), the back-EMF (computed as a function of motor speed) and the current supplied to the motor. Internal resistance of the battery – source path and the MOSFET resistance in the motor drive are included as they are important factors in the model. This model, once validated, is a step towards meeting the needs of both open loop torque control and touchdown sensing. The pronking controller discussed in subsequent chapters relies on the current model presented here for its touchdown detection.

Component Models and Assumptions

RHex's actuators are six locked anti-phase modulated H-bridges connected through LC low pass filters to Maxon RE118751 "ironless" brushed DC motors. The Motors are subsequently connected through 33 1/16:1 planetary gear heads to the legs.

The analysis begins with the simplest models possible for the drive and motor. In the case of the drive, this model is validated analytically, by showing that the simplified model closely approximates a more detailed analytic model of the drive. The gear is not modelled or tested in this work.

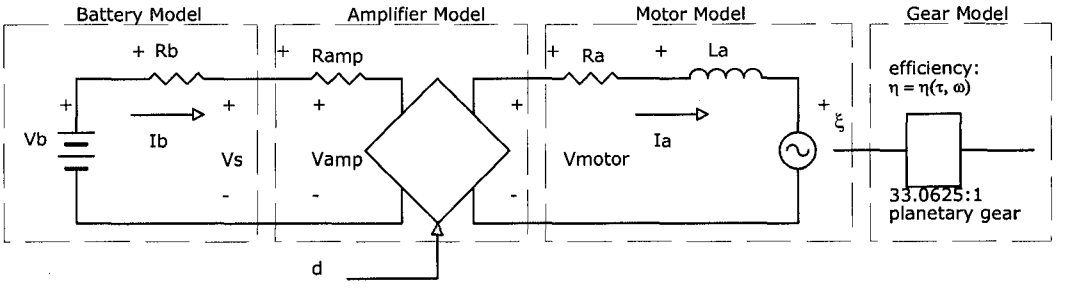

Figure 6: Ciruit diagram for battery / amplifier / motor / gear combination

We begin with a circuit model, treating the SA60 module as an ideal DC transformer with an input resistance R_{amp}. Normally the PWM amplifier would be modelled together with the motor, as the winding inductance of the motor is a necessary part of the step down converter circuit, filtering out the PWM carrier frequency to produce a smooth voltage output. However, in this application an LC low-pass filter with roll-off frequency 8.4 kHz attenuates the 100 kHz PWM carrier frequency, so that the output may be modeled as a voltage proportional to the duty factor and supply voltage. Figure 7 shows the output stage of the amplifier, filter and motor.

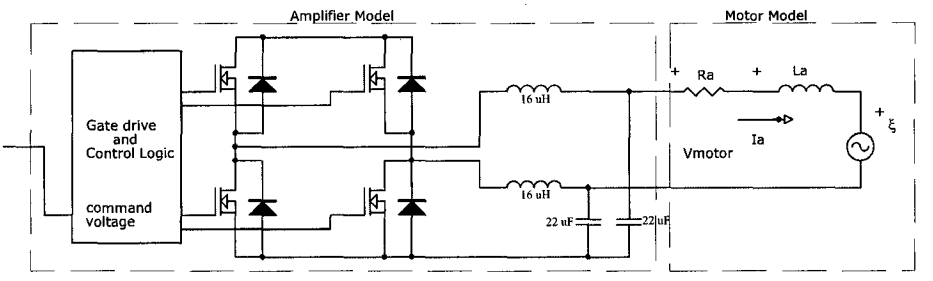

Figure 7: Detail of amplifier, output filter and motor

This ideal transformer model gives $V_{motor} = V_{amp} \cdot d$, where d is the control input (duty cycle) from the computer.

Beginning with the secondary side of the transformer, the loop current may be solved by means of Kirchoff's law:

$$I_a = \frac{V_{motor} - \xi - L_a \frac{dI_a}{dt}}{R_a} \quad (1)$$

Next, a simple resistive model is used for both the battery and the voltage drop caused by the drive MOSFETs (R_{amp}).

$$V_{amp} = V_b - R_b I_b - R_{amp} I_b \quad (2)$$

$$V_{motor} = d \cdot V_{amp} = d(V_b - R_b I_b - R_{amp} I_b) \quad (3)$$

$$I_a = \frac{d(V_b - R_b I_b - R_{amp} i_b) - \xi - L_a \frac{dI_a}{dt}}{R_a} \quad (4)$$

But $I_b \cdot V_{amp} \cong V_a \cdot I_a$, assuming efficient (< 5 % loss) power conversion and $V_{motor} = d \cdot V_{amp}$, so

$$I_b = d \cdot I_{motor} \quad (5)$$

$$I_a = \frac{d \cdot (V_b - R_b \cdot d \cdot I_a - R_{amp} \cdot d \cdot I_a) - \xi - L_a \frac{dI_a}{dt}}{R_a} \tag{6}$$

$$I_a R_a = d \cdot V_b - d^2 \cdot R_b I_a - d^2 \cdot R_{amp} I_a - \xi - L_a \frac{dI_a}{dt} \tag{7}$$

$$I_a (R_a + d^2 \cdot R_b + d^2 \cdot R_{amp}) = d \cdot V_b - \xi - L_a \frac{dI_a}{dt} \tag{8}$$

$$I_a = \frac{d \cdot V_b - \xi - L_a \frac{dI_a}{dt}}{(R_a + d^2 \cdot (R_b + R_{amp}))} \tag{9}$$

This model is a complete expression for the motor current given the assumptions outlined above.

At this point, several approximations are made to simplify the model:

$$d << 1;$$
$$R_a > 1;$$
$$L_a \frac{dI_a}{dt} << \text{Other terms};$$

The model can be further simplified since the voltage at the input of the motor drive (V_s) is known from data acquisition. As well, back EMF, ξ, is given by $\xi = K_s \omega_a$. These simplifications result in the following model.

$$I_a \cong \frac{d \cdot V_s - K_s \omega_a}{R_a + d^2 R_{apex}} \tag{10}$$

where K_s is the datasheet value of the motor speed constant; R_{amp} is given by the SA60 datasheet; and R_a is given by the motor datasheet. V_{amp} is measured with the onboard voltage battery terminal voltage measurement, and d is known since it is proportional to the DAC command voltage.

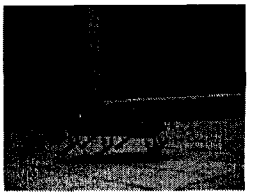

2.3 Motor Model Validation

The model given above was tested in the robot with one minor difference. The resistance of the MOSFETS was modelled as part of the secondary of the transformer circuit given in Figure 6. This may account for some of the error observed in the experimental results.

The model parameters used in the experimental validation are summarized as follows.

Parameter	Datasheet Value	Units
Speed constant	61.26	(rad/s)/V
R_a	1.33	Ω
R_{apex}	0.45	Ω

Table 1: Parameters for the motor current estimation model

To test the motor / drive model on the robot, a Honeywell CSLB1AD [17] Hall-effect current measurement device was fitted to the robot and connected to the robot's onboard data acquisition system (a MicroSys MPC550 [18] analog/digital I/O card).

The current measured by RHex's data acquisition was compared to the estimate provided by the model described above during a short sequence of walking and pronking. Results of the experiment are shown in Figure 8 and Figure 9. Happily, this simple model shows reasonably good estimation of the actual motor current. RMS current error during walking was 0.68 A or 6.8 % of full-scale (we take full-scale to be the maximum continuous motor current supplied by the drive, 10 A). During the more strenuous pronking run, the RMS current error was 0.87 A or 8.7 % FS.

Interestingly, both plots show a strong correlation between error and motor current. By performing a linear regression on the data, the results can be improved slightly. Figure 10 and Figure 11 show the same data when a linear regression is used to correct the model. For both runs the regression coefficient was between 0.8 and 0.82. Error performance improves incrementally with this "fudge" factor: 0.57 A error RMS or 5.7 % for walking and 0.75 A or 7.5 % RMS error for pronking.

Sources of error

It is worthy of note that to expedite this preliminary motor modelling effort little time was spent finding a high performance current sensor. The Honeywell CSLB1AD exhibited poor noise performance when installed in the robot— appearing to be very sensitive to power supply noise. As installed, the sensor typically gave up to 0.32 A RMS error. To illustrate the noise level, a plot of the sensor output while measuring a 5.0 A constant current is shown in Figure 12. The source of this high level of noise was not found (it was very likely due to either power supply problems or analog-to-digital converter noise), but these results are likely to be replaced in future work with more accurate dynamometer measurements.

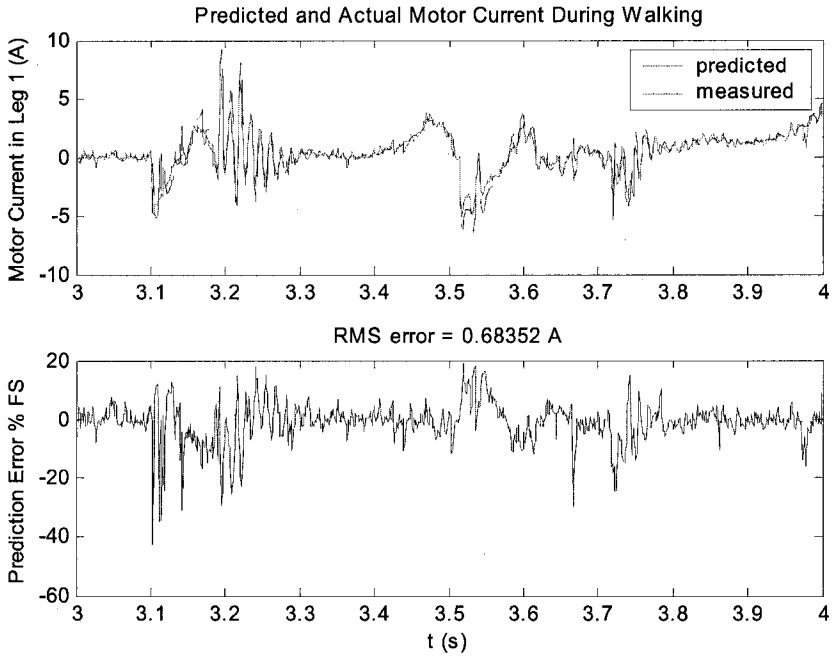

Figure 8: Validation of Motor Model During Walking

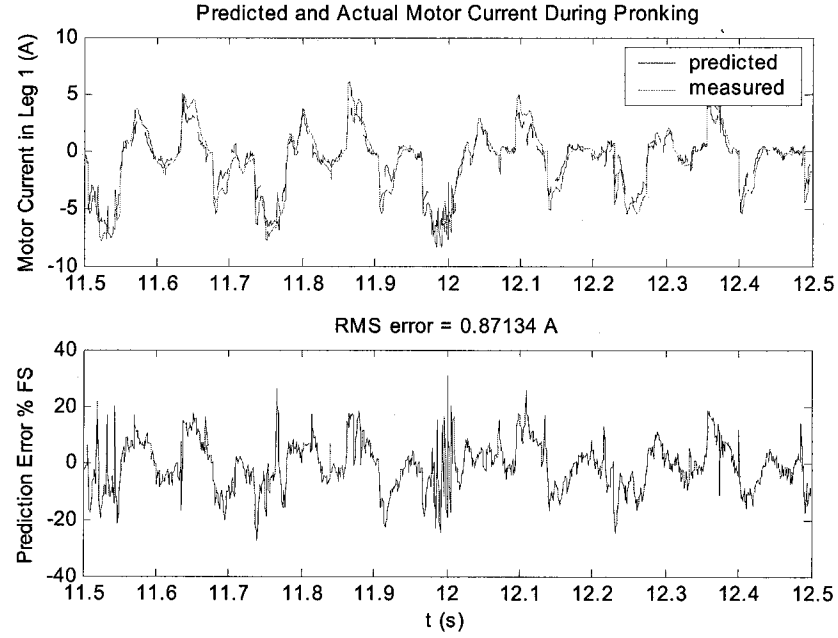

Figure 9: Validation of Motor Model During Pronking

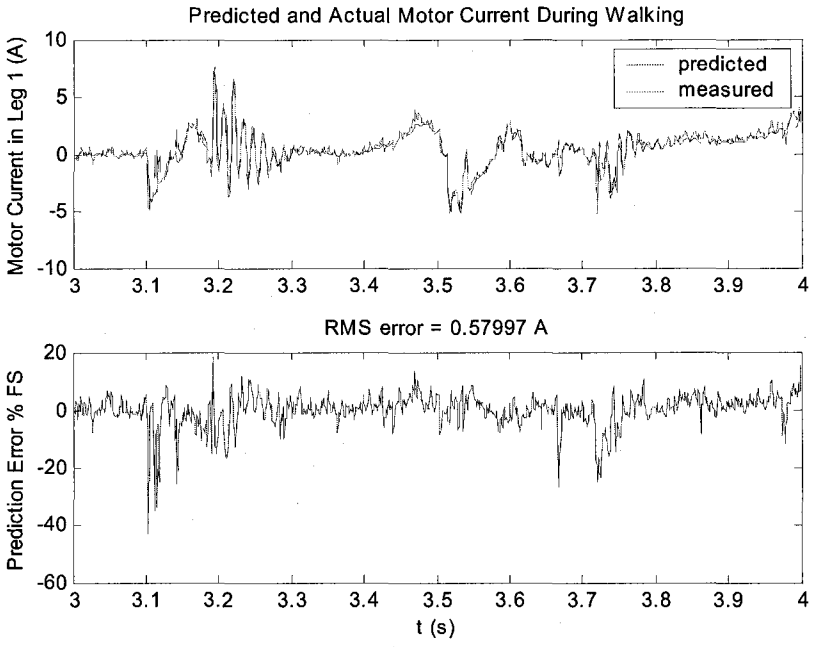

Figure 10: Improved fit using linear regression

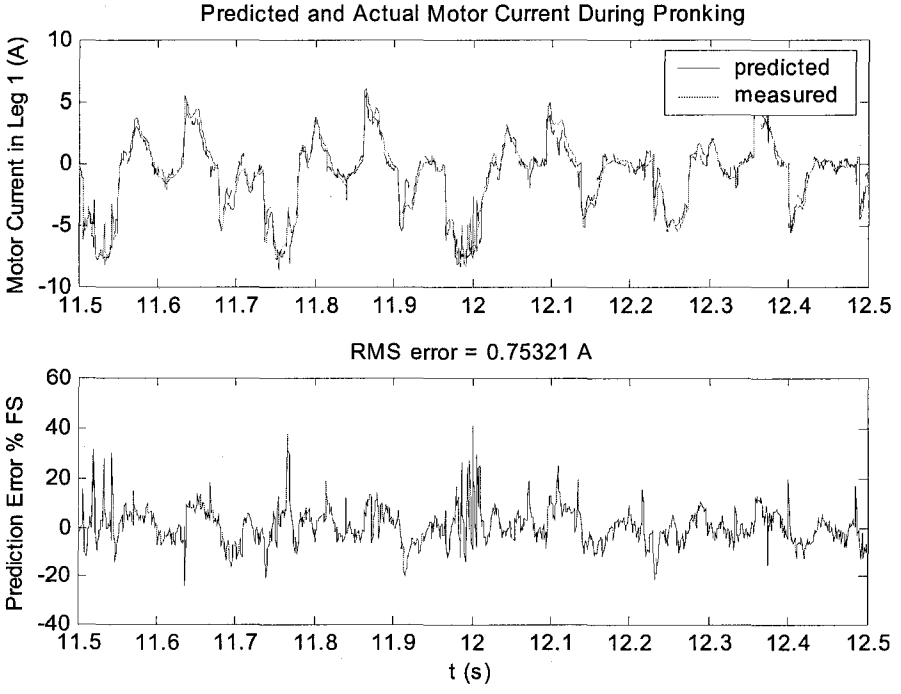

Figure 11: Improved fit using linear regression

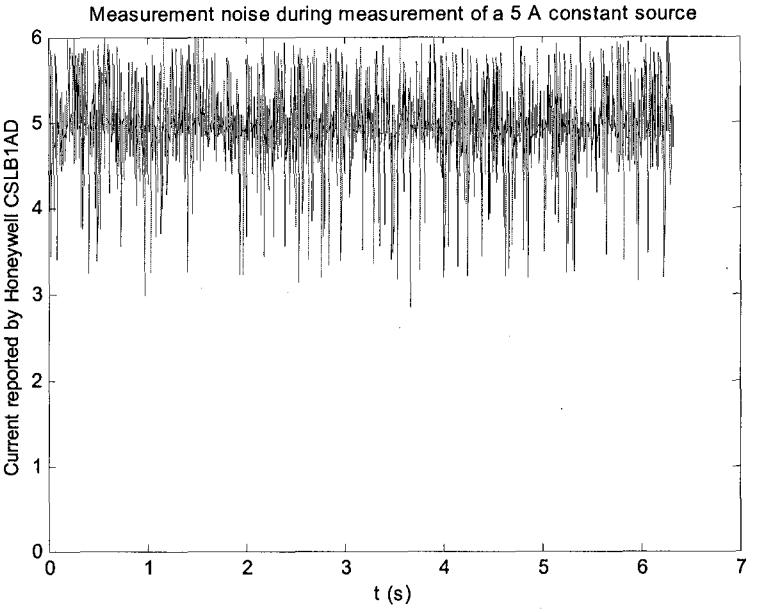

Figure 12: Measurement noise observed during measurement of a 5.0 A source

Conclusions and Future Work

Validation of the simple DC motor model described above produced surprisingly good results. 7.5 % RMS error was obtained during pronking—good enough performance to motivate the construction of a touchdown detection algorithm based solely on the estimates of motor current (and hence leg torque).

Future work in modelling the RHex motors is already underway at the ARL with the construction of the RHex dynamometer. This dynamometer setup consists of a RHex motor and a larger, more powerful, load motor coupled through a torque measurement apparatus. Temperature, motor current and voltage and various other quantities are being measured. With this new experimental setup, we hope to be

able to model motor current and leg torque within 5 % of full-scale over all conditions.

2.4 Motor Drive Redesign

At the beginning of this work, the motor driver board on RHex was bulky, heavy, and prone to spectacular failures (sometimes involving smoke and fireworks). Though this board providing an unprecedented power density (over 1000 W peak could be delivered to RHex's motors), it clearly needed some improvement. The redesign of this board was performed with the goal of preserving the existing performance and improving weight, size and reliability.

To understand fully the design decisions made in the construction of the MD v 1.1 motor drive, some initial analysis and experimentation was required. The results of this are covered in the next section, and serve as an introduction to the challenges of the motor driver design for RHex.

The starting point

The first version of RHex, "RHex-0" was fitted with an MD v1.1 motor driver board, designed by Uluc Saranli and Martin Buehler. This board was the workhorse of the robot, supplying up to 15 A peak to each of six low-inductance DC motors. The motor driver board was built around the Apex Microtechnology SA60 [19] hybrid motor driver circuit, six LC-lowpass filters and a handful of support components.

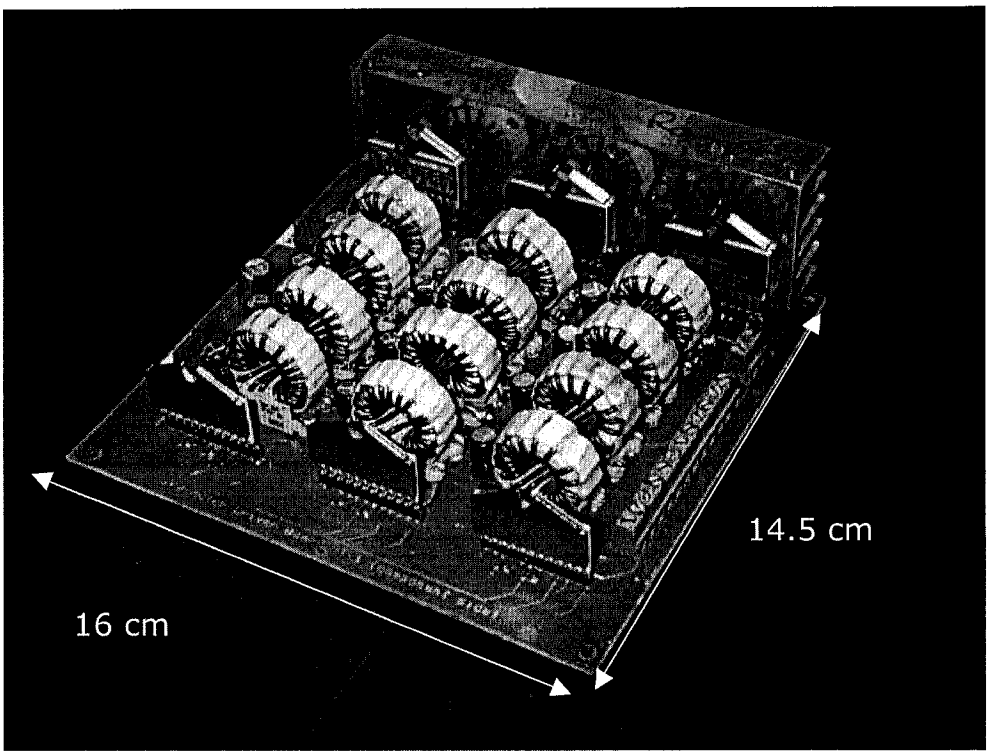

Figure 13: RHex Motor Driver Board v 1.1 (front heatsink removed)

This design was the first version, and therefore had some shortcomings—principally reliability and weight (750 g with heatsinks). Circuit board trace failures were common when the robot was running under stress, and occasionally the SA60 modules became unseated from their sockets. The board initially carried two heat sinks (one on either side) made from 1/16" aluminum sheet. On long runs, the SA60 modules would heat up, and occasionally this lead to failures. Furthermore, as the Apex SA60 was a proprietary design with no information about the internal control topology, the drive was not well understood or modelled. Though the SA60 was thought to be efficient, the drive drew substantial power at standby (when the motors were not under load), raising questions about actual efficiency of the motor drive system.

To improve the design, three key areas were therefore addressed: reliability (mechanical, electrical and thermal), modelling and characterization and efficiency.

PWM drive topologies for DC motor control

A motor driver provides the means to modulate power applied at an actuator. Modulation in this case means being able to control both the magnitude and the sign of either the current or voltage applied to the motor terminals. For reasons of efficiency, this is performed using MOSFET transistors driven in "switch mode" so that they are either fully on (very low resistance, hence low power dissipation) or fully off (open-circuit; no power dissipation). There are many topologies for modulating the current in a motor using an H-Bridge. The two most basic, "unipolar modulation" and "locked anti-phase modulation" are shown in Figure 15 below.

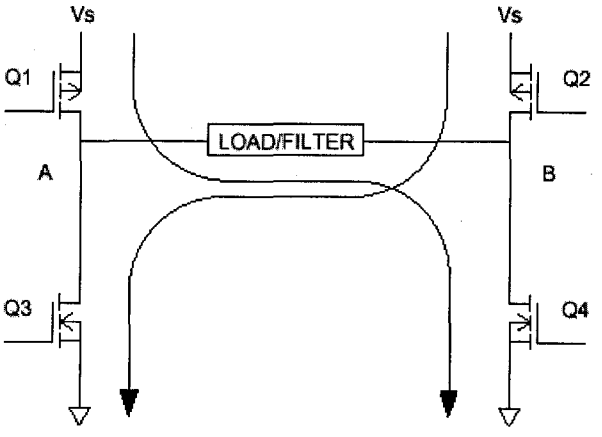

Figure 14: PWM H-Bridge used to modulate sign and magnitude of voltage applied to motor.

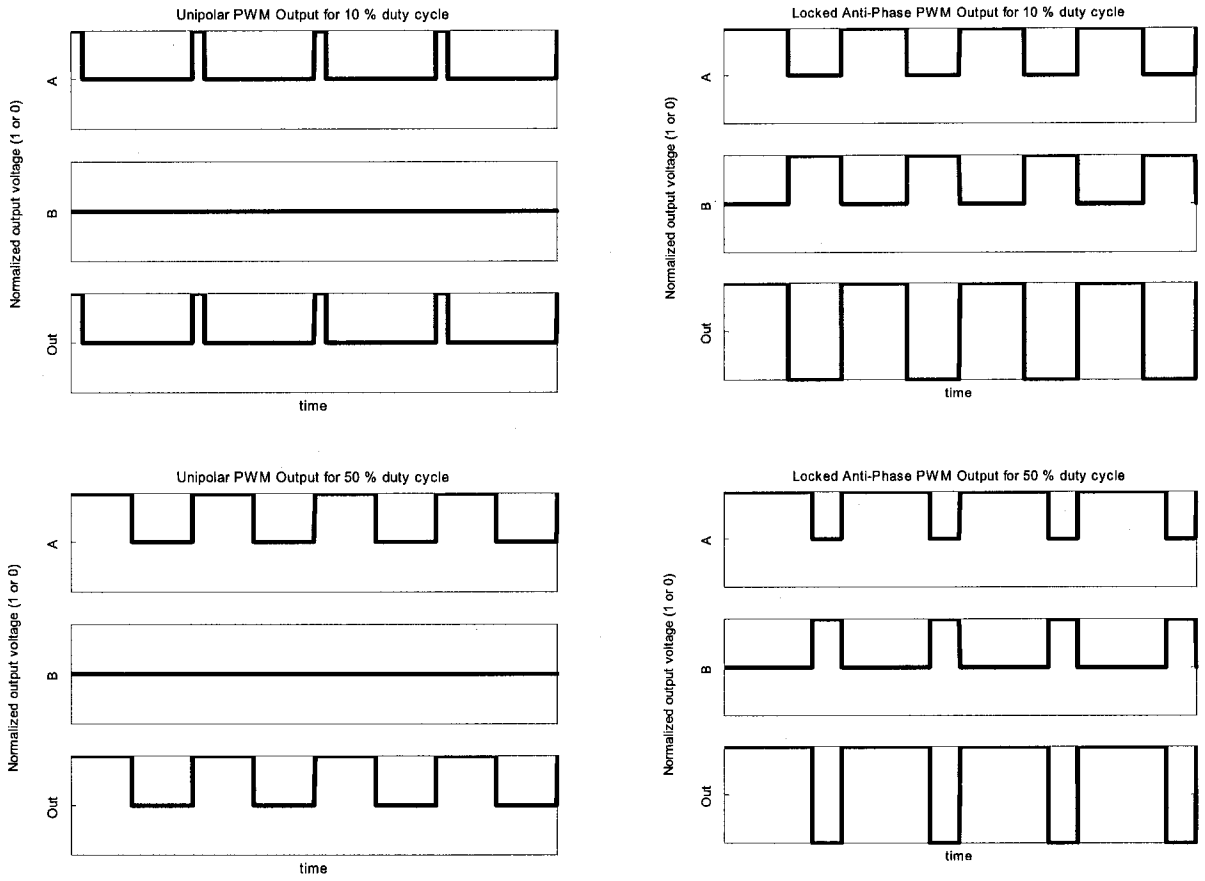

Figure 15: Comparison of output voltage waveforms for unipolar and locked anti-phase PWM

Note that for the same duty cycle, d, (taken to be $\in$ [-1, 1]) each topology delivers an output voltage with average $d*V_s$ as the difference between its A and B phase outputs. However, a readily observed, yet startling, feature of the locked anti-phase topology is that the RMS voltage between the outputs is V_s, whereas with the unipolar topology the RMS output votlage is $\sqrt{|d|}V_s$. As a result, this drive may deliver substantial power to a load even when the duty cycle is zero. To drive a motor from a locked anti-phase drive, one must clearly filter out the PWM carrier signal to remove the AC component of the waveform.

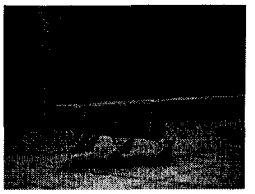

The SA60 Module: a motor driver on a chip

The Apex SA60 is a hybrid module* containing a high-efficiency, all-in-one class D amplifier. There are two main components to this device: the PWM control and gate drive, and the MOSFET H-Bridge. A block diagram for the SA60 module is shown in Figure 16. The unit operates in locked anti-phase modulation mode, meaning that the output voltage reverses polarity twice per PWM cycle. Figure 17 shows experimentally the result of naively connecting a this bipolar output signal directly to a motor. Because the duty cycle is ~50%, the voltage and current waveforms are close to symmetric across the abscissa and the average current is close to zero (the motor shaft does not rotate). Yet 1.0 A RMS are being delivered to the motor (14.2 W mean), resulting in rapid temperature rise at the motor. If one were to connect all six of RHex's motors without amplifiers, the average power draw with the legs applying zero torque would therefore be over 85 W!

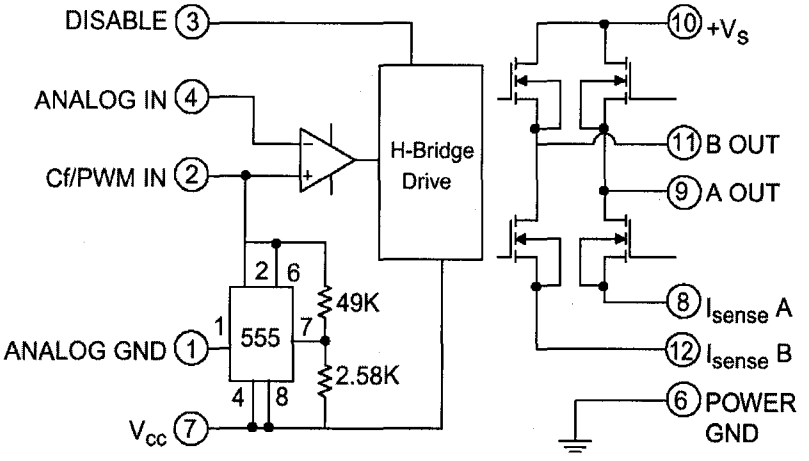

Figure 16: Block diagram for the SA60 module

---

* A circuit constructed from SMT components wire-bonded to a ceramic (in this case BeO_2) substrate.

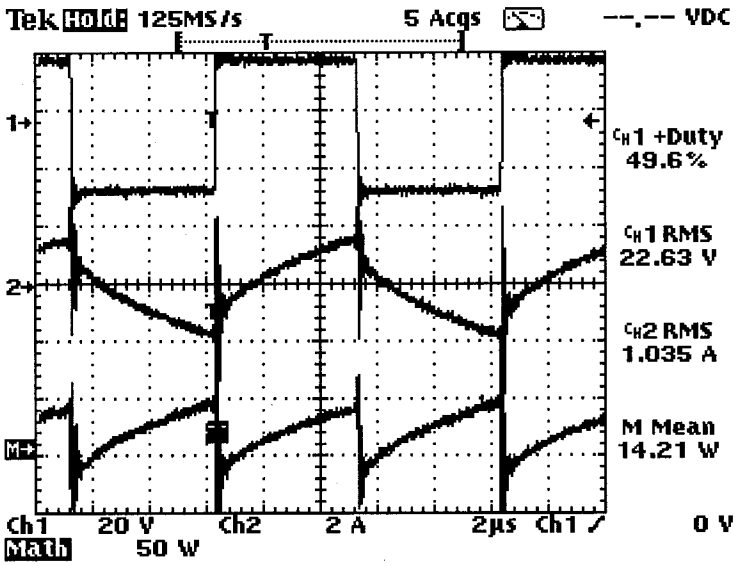

Figure 17: Output voltage, current and power for SA60 module connected directly to a Maxon RE118751 motor.

Obviously this is not the configuration intended by the manufacturer for the control of a low-inductance motor such as the RE118751. Instead, Apex recommends that for low inductance motors an L-C low-pass filter be placed between the SA60 module and its load, when the load inductance is less than 300 µH.

PWM Drive Efficiency: Single ended vs Bipolar

Though efficiency was not the primary focus of the motor driver design, it is an important factor in any robot motor drive since higher efficiency equates with longer runtime and hence greater utility. The massive power dissipation resulting from naively connecting the bipolar SA60 PWM drive to a motor led the author to consider carefully, and experiment with, low-pass filter designs and alternative PWM drive topologies. Conversion efficiency was measured for two different low-

pass filter designs on both single ended and bipolar drives and is discussed in the efficiency comparison section.

Original Low-pass filter design

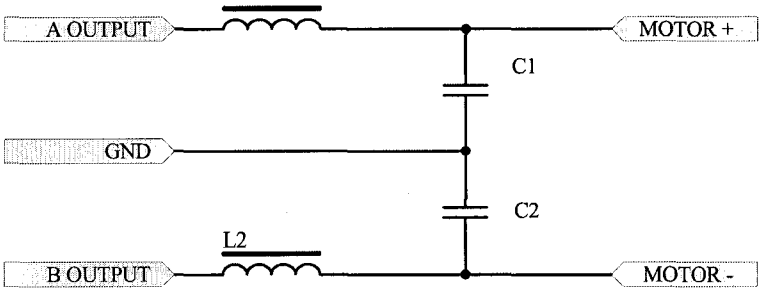

Figure 18: Schematic for motor drive second-order low pass filter

To minimize ripple current in the motor, Apex recommends [20] adding a low-pass filter, such as the one shown in Figure 18, between the output of the drive and the motor itself, with a roll-off frequency, f_c of 10 % or less of the switching carrier frequency (100 kHz). The motor is a Maxon RE118751 coreless DC motor with 120 µH winding inductance and 1.3 Ω winding resistance; its roll-off frequency is given by:

$$f_c = \frac{1}{2\pi}\left(\frac{L}{R}\right)^{-1} = \frac{1}{2\pi}\left(\frac{120\mu H}{1.3\Omega}\right)^{-1} = 1724\,\text{Hz} \qquad (11)$$

In order to minimize the weight of the filter, while still adhering to the filter design guidelines set out in [20], a 25 µH inductor and 22 µF non-polar capacitor were selected so that:

$$f_c = \frac{1}{2\pi}\left(\frac{1}{\sqrt{LC}}\right) = \frac{1}{2\pi}\left(\frac{1}{\sqrt{22\mu F \cdot 25\mu H}}\right) = 6786\text{Hz} \qquad (12)$$

This roll-off frequency is 6.8 % of the carrier frequency of 100 kHz.

The inductor selected was a J W Miller 6706 toroidal power inductor, rated for 9 A [21]. Using the Apex filter design application note [20] a

maximum ripple current of 9 % of the full-scale output current was predicted for this filter-motor combination.

With the filter in place, the voltage, current and power at the motor terminals was as follows:

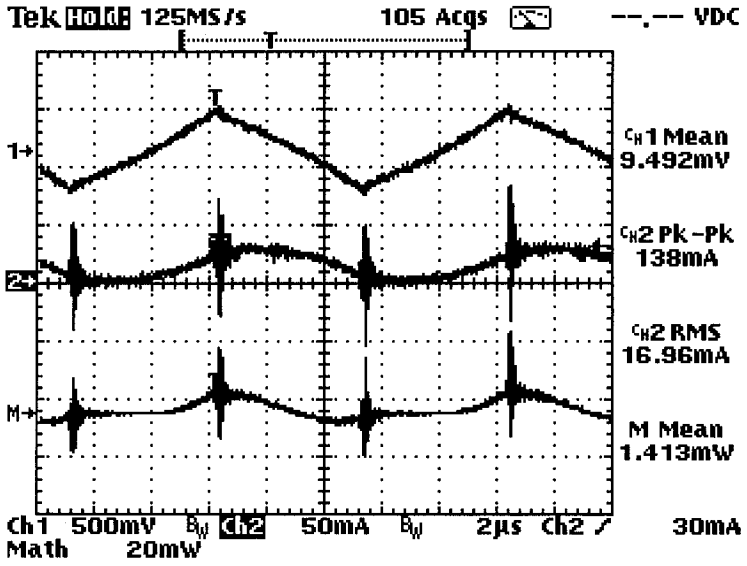

Figure 19: Output voltage current and power for the SA60 module driving a motor via the L-C low-pass filter (JW Miller inductors)

The dramatic decrease in ripple current shown in Figure 19 confirms the utility of low-pass filtering to remove the PWM carrier and its harmonics. In this case the RMS ripple current is reduced to 17 mA, or 1.6 % of the value measured in Figure 17. Total power dissipation in six motors applying zero torque would now be approximately 8 mW (though substantial current still flows through the amplifier MOSFETs and there is still power dissipation due to this).

Component Selection

Although the low-pass filter used in the v 1.1 drive performed adequately, the total weight of the inductors alone used on the board

was 300 g (4 % of the robot's mass of 7.5 kg). In order to improve the weight and size of the board, a smaller inductor had to be found. In searching for such an inductor, it was first recognized that the actual inductance of the filter inductor at 100 kHz and at high current was probably much lower than the value given by its datasheet, which was measured at 1 kHz. For this reason, inductors designed for high-frequency, high power switching applications were considered in preference to ones with higher inductance but poorer high-frequency credentials.

Due to its small size and inductance rating at 100 kHz, the Panasonic ETQ-P6F8R2HFA was selected for evaluation. As this inductor was rated at only 10 μH, two inductors were put in series to double the inductance. To ensure comparable performance with this new inductor, a motor ripple current test was performed in comparison with the J. W. Miller part mentioned earlier at 50 % duty cycle, from a 24.0 V supply. The experimental setup for this comparison was shown below. A low-pass filter module constructed from each type of inductor was used where the low-pass filter block is indicated.

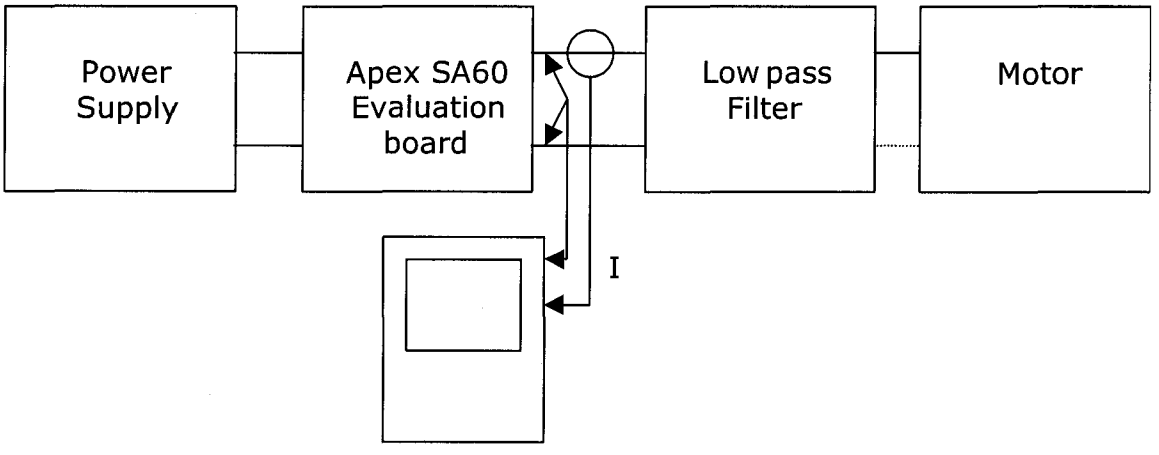

Figure 20: Setup for Motor driver efficiency testing

The results of this experiment are shown in Table 2. Interestingly, the 20 μH combination of Panasonic inductors output perform the 25 μH J. W. Miller inductors, reducing the power at zero torque (50% duty) by nearly half.

Table 2: Table 2: Results of the ripple current comparison at 0 % duty cycle

Inductor Type	Ripple Current (RMS mA)	24 V Power Supply Draw (mA)
No filter	1030	735
J. W. Miller 25 μH	17	165
Panasonic 8R2 10 μH	7.9	197
2 X 8R2 (20 μH)	4.2	99

Thermal support

To improve the reliability of RHex's motor driver board, care was taken to ensure adequate thermal support for the SA60 modules. At the maximum continuous current of 10 A, each SA60 module may generate as much as 75 W in heat. To avoid drastic reduction of lifetime, the junction temperature in MOSFETs on each module must be kept below 165 °C. Although one could in principle solve the heat sink problem with an arbitrarily large heat sink, we are obviously only interested in solutions which are as lightweight as possible while still meeting the required thermal specifications.

Thermal support overview

Exact modelling of the flow of heat from a power semiconductor typically involves either solution of analytic boundary value problems, or modelling with finite-element thermal analysis software. These techniques provide more precision and complexity than is required in the basic design of a heat sink. For this reason, heat flow from a power

semiconductor is approximated using aggregate thermal resistance values (°C/W), which, when multiplied with the heat (W) flowing from the device, allow a reasonable estimate of the thermal rise across an interface. Figure 21 illustrates the important interfaces in our design problem:

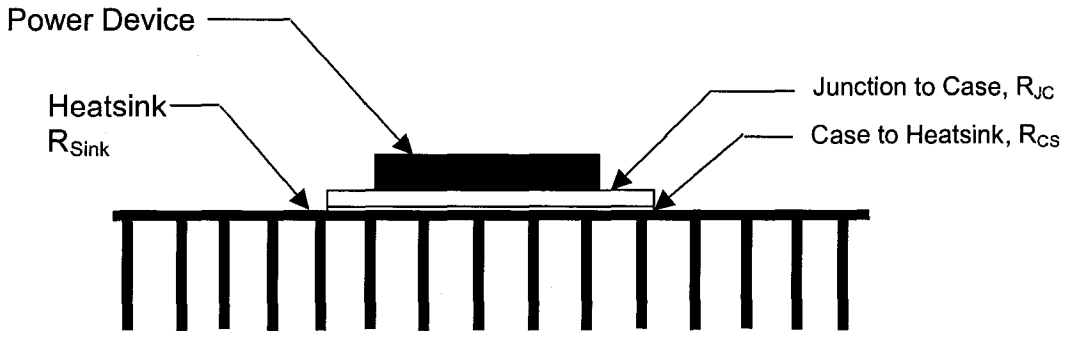

Figure 21: Important interfaces for SA60 heat flow

Apex Microtechnology publishes a R_{JC} of 1.6 °C/W [19], and also reports an R_{CS} of 0.2 °C/W using zinc-oxide/silicone thermal compound, or their special thermal washers (Apex P/N TW07). It should be noted that the values for the case-to-sink interface are quoted for specific minimum torques – pressure is an important consideration between the case and heat sink.

The heat sink selection method used was as follows:

- Estimate the maximum possible current at the highest operating temperature.
- Based on this, look up total voltage drop and calculate total heat generated (Q).
- Using a maximum junction temperature of 150 °C, and an ambient temperature of 40 °C, calculate the required heat sink thermal impedance as follows:

$$R_{Sink} = (150\ °C - 40\ °C)/Q - R_{JC} - R_{CS} \qquad (13)$$

Alternately, one may design based on a maximum case temperature (and this constraint must be met in either case):

$$R_{Sink} = (85\ °C - 40\ °C)/Q - R_{CS}$$

Achievable R_{Sink} values will be in the range of 1.5 – 5 for a natural-air cooled sink or 0.2 – 0.9 for a forced-air cooled sink. If possible, forced-air heat sinks should be avoided due to (1) the resulting dependence on the reliability of a fan and (2) the added noise and current consumption associated with fans.

Design Calculations

Using the equations above, and with a measured R_{CS} of 0.22 °C/W, a target thermal resistance of 0.34 °C/W was obtained, based on a total power dissipation of 80 W. This thermal impedance is clearly well into the range of forced-air cooled sinks, and is likely below what can be obtained with a reasonably sized heat sink. However, it is important to note that the calculations apply to steady-state currents of 10 A, and in our application the steady state current should be much lower than this.

Experiments

The design of the heat sink was tested prior to construction using an extrusion of similar dimensions to those of the desired heat sink. For the forced air tests, a 1 W box fan was affixed transversely to the sink. It was noted that air flow away from the sink was strongest at the ends (ie. the air flow was excellent in this configuration). For all tests a Powerex KSF24505 850 V, 50 A power Darlington module was run in linear mode while bolted to the sink with zinc-oxide/silicone thermal paste in between. Base current was set from a 5 V supply using a 1 kΩ potentiometer, while power was supplied to the device from a variable voltge/current supply (set to limit at 10 V and 5.5 A). The potentiometer was adjusted so that the dissipated power for the device was 50 W. For all tests the ambient temperature was 27 °C.

The results of the experiments are summarized in the table below:

Table 3 : Results of heatsink testing with 50 W source

Convection	T_{Sink} (°C)	T_{Case} (°C)	T_{Amb} (°C)	Q (W)	R_{CS} (°C/W)	R_{Sink} (°C/W)
Natural	93	104	27	50	0.22	1.32
Forced	60	69	27	50	0.18	0.66

Conclusion

The calculations and experiments detailed above resulted in the design and construction of a heat sink used on RHex with the v 1.1 motor driver board for roughly one year. During this time, no failures due to overheating were observed (ie. all failures were clearly attributable to other causes). Although these thermal design considerations do not predict the transient thermal response, they provide an excellent

yardstick for how well the SA60 module is being cooled with a particular heat sink.

Edward Moore continued this work with the design of another passive-cooled heat sink for the v 1.3 motor driver board [22].

MD v1.3 Driver Board Layout

As the culmination of the information gathered in the preceding sections, a board was designed to replace the MD v 1.1 motor driver boards. The objective of this board design was to replace the v 1.1 board with a similar circuit while improving the size, mass and reliability of the board.

Though this design will not be discussed here in detail, improvements were made in the following areas:

- tighter integration of components to reduce heat sink mass
- reduction of mass from 534 g to 215 g for board (without heat sink)
- no trace failures have been observed with the new board

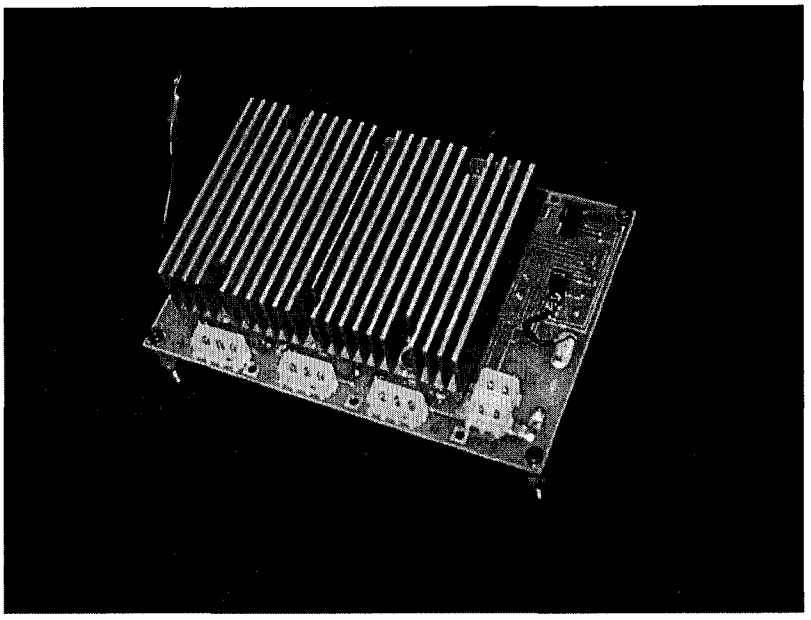

Figure 22: The complete v 1.3 motor driver board

2.5 Conclusions and Future Work

This chapter described the characterization and redesign of RHex's motor drivers. A simple model of motor current provides estimates of current within 7.5 % RMS during pronking. Thermal dissipation performance was improved by an empirical heat sink redesign. Subsequently, the only thermal failures of SA60 modules on RHex have been due to jammed or burned motors shorting the SA60 modules for long periods of time. A new motor driver board was also designed which weighs less than 50 % that of the old design.

Chapter 3 An Attitude Estimator for RHex

3.1 Motivation

Management of robot body attitude (particularly pitch) during pronking appears to be a key factor for stability. To permit the measurement and control of this variable, an attitude estimation system was required to measure precisely and repeatably the attitude of the robot with respect to the (fixed) horizontal plane during pronking. Any hardware considered for this problem had to fit in the robot along with existing robot components. This imposed severe size and power consumption constraints.

3.2 Technologies available

To facilitate the estimation of body pitch, several technologies were considered, including the ground-directed distance sensors similar to those used by ARL's Scout II [23], and various inertial sensors available on the market.

Ground-directed distance sensors

By measuring the distance to the ground at either end of the robot, together with the assumption that the ground is flat, one can easily obtain an estimate of the relative body pitch of the robot.

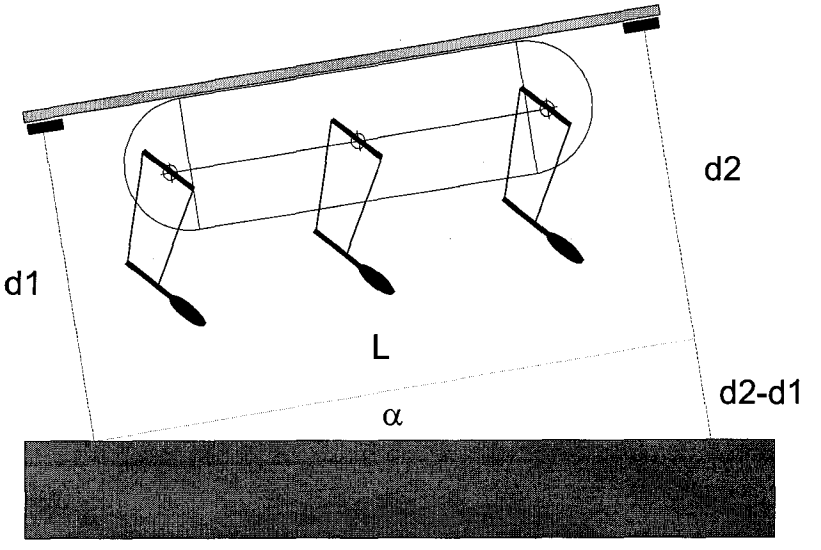

Figure 23: Body pitch estimation using ground-directed distance sensors. The pitch angle, α, is given by atan(d2-d1/ L).

This method has been used on ARL's Scout II robot to measure body pitch with two Aromat triangulation laser range finders. To test it on RHex, a setup was built with two Sharp GP2D12 IR triangulation sensors. Accurate, albeit low-bandwidth, pitch information was obtained with these sensors so long as they remained in range. However, due to the reliance on the assumption of flat ground this method of pitch measurement was not acceptable.

Testing of this method of pitch measurement was accomplished by mounting RHex on its side with the middle motor shaft clamped and the Sharp IR ranging sensors pointing horizontally toward a vertical plywood board. In this manner the measurement of pitch obtained from the range sensors could be compared directly to the 'ground truth' measurement obtained from the motor's optical encoder. Figure 24 shows the performance qualitatively: the sensors are noisy, have a low sampling rate and would require individual calibration to produce consistent output.

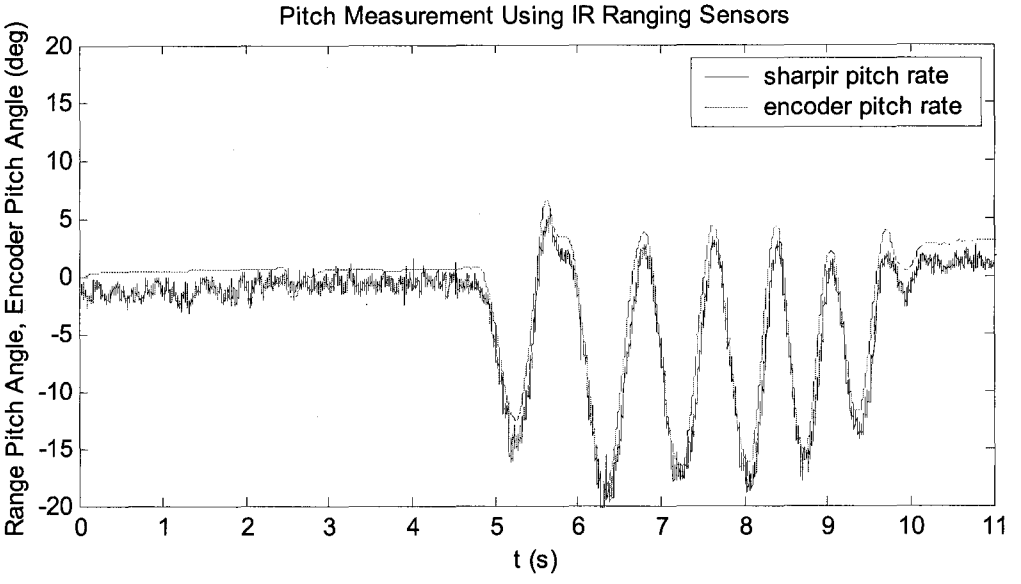

Figure 24: Evaluating the performance of Sharp GP2D12 IR ranging sensors for pitch measurement. Noisy line is pitch estimated from Sharp sensors as compared to encoder ground truth pitch measurement (smooth line).

3.3 Inertial Attitude Estimation

An alternative to ground-directed distance measurement is inertial attitude estimation. As both aircraft and satellites rely on inertial sensing for attitude estimation there is a mature literature on the kinematics of inertial sensing as well as the sensors themselves. The rotation rate sensors used in inertial systems tend to be of one of three types of gyroscopes: mechanical (spinning), Coriolis effect and laser interferometer.

Mechanical gyroscopes have been used the longest for attitude estimation in aircraft and other vehicles. Despite their success in numerous applications they were not considered for RHex due to the promise of smaller, cheaper Coriolis-effect and laser gyros. Figure 25a

shows an exemplar of the mechanical family of gyros, a Litton G-2000 gyroscope, weighing just 20g and measuring roughly 2 X 2 X 2.5 cm.

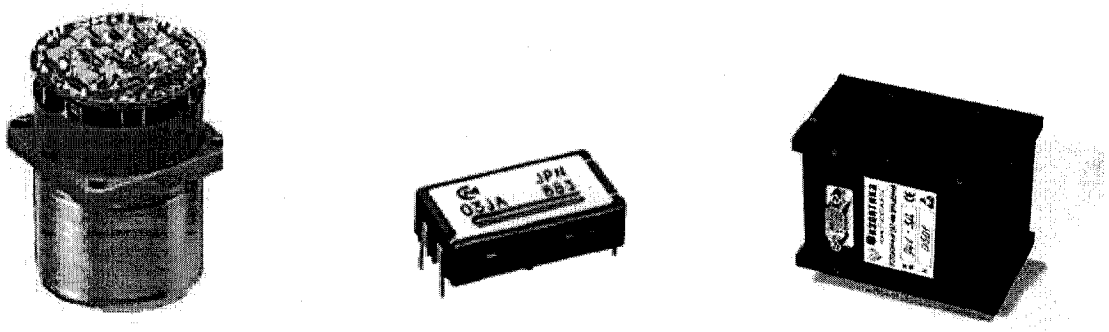

Figure 25a,b,c: Left to right Litton G-2000 mechanical gyro [24], Murata ENC-03J Coriolis force gyro [30], Fizoptika VG941-3D Fibre-optic laser ring gyro [33]. Images are from the respective corporate websites. Figure not to scale.

Coriolis-effect gyro

Coriolis effect gyros, such as the popular Murata ENC and ENV series offer small size and power consumption, though perhaps the poorest performance. The Murata Coriolis-effect gyroscopes are built around a vibrating prism, as shown in Figure 26. The prism is driven at its resonant frequency from one side by a piezoelectric element and is free to vibrate horizontally or vertically. When the prism, and hence the gyro, is rotated about its longitudal axis, the vibrations being driven on the vertical axis (for example) will couple onto the horizontal axis. The coupled vibrations are picked up on the secondary axis by a second piezoelectric transducer. The amplitude and phase of the measured oscillations indicate the speed and direction of rotation.

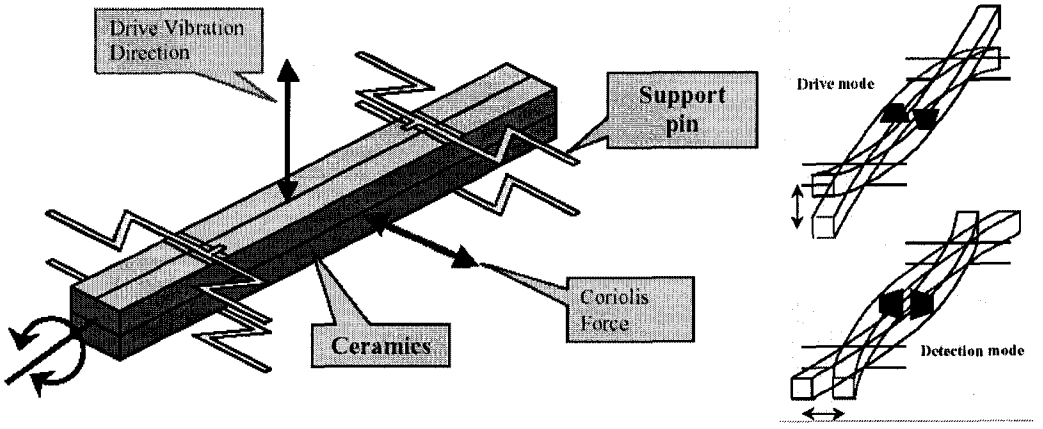

Figure 26: Diagram of prism mechanical oscillator (illustrations courtesy Murata)

Murata ENC-03J

The Murata ENC-03J (shown in Figure 25b) offers +/- 300 deg/s dynamic range in a tiny (15 X 8 X 4.5 mm) package. Its output is an analog voltage proportional to the rotation rate (scale factor = 3 mV/(deg/s)). Linearity is 5% of full-scale, and no compensation model is given. This sensor is intended for applications where angular rate may be filtered by a high-pass filter, such as vibration tables and image stabilization systems. Due to the need for an estimate of attitude that may include steady-state changes in orientation (ie. non-zero mean inputs to the gyro), the high-pass filter circuit could not be used in this application. High-pass filters, such as the one specified in the ENC-03J datasheet, entirely remove any zero-frequency components, generating an output which is always zero mean. Under periodic oscillations of a frequency much greater than the roll-off of the filter, this arrangement would allow correct measurement of angular rate. However, non-zero mean changes in angular rate would have their zero-mean components removed. Since the gyro is intended to drive a high-pass filter, bias

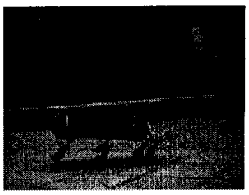

stability and repeatability are not specified; experiments showed that the bias rate varies wildly between successive experiments, making the sensor unsuitable for this application. Figure 27 and Figure 28 show a ground-truth comparison experiment using the integrated output of the gyro to estimate robot pitch; the robot is constrained to rotate only about the pitch axis during the experiment. The average output of the gyro for a one second period at the beginning of the experiment is used to estimate the bias rate for the integration.

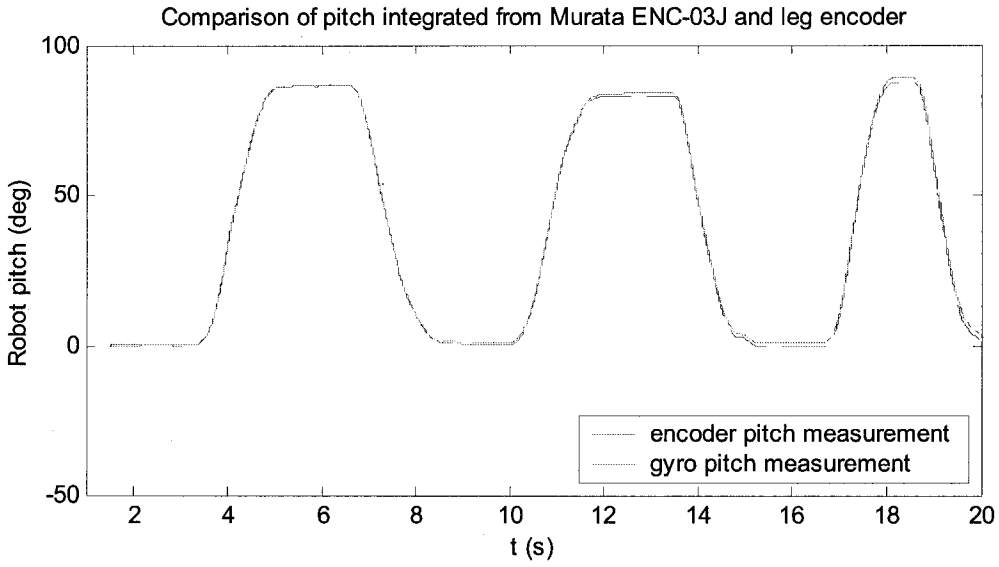

Figure 27: Evaluating the performance of the ENC-03J piezoelectric rate gyroscope

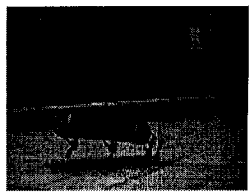

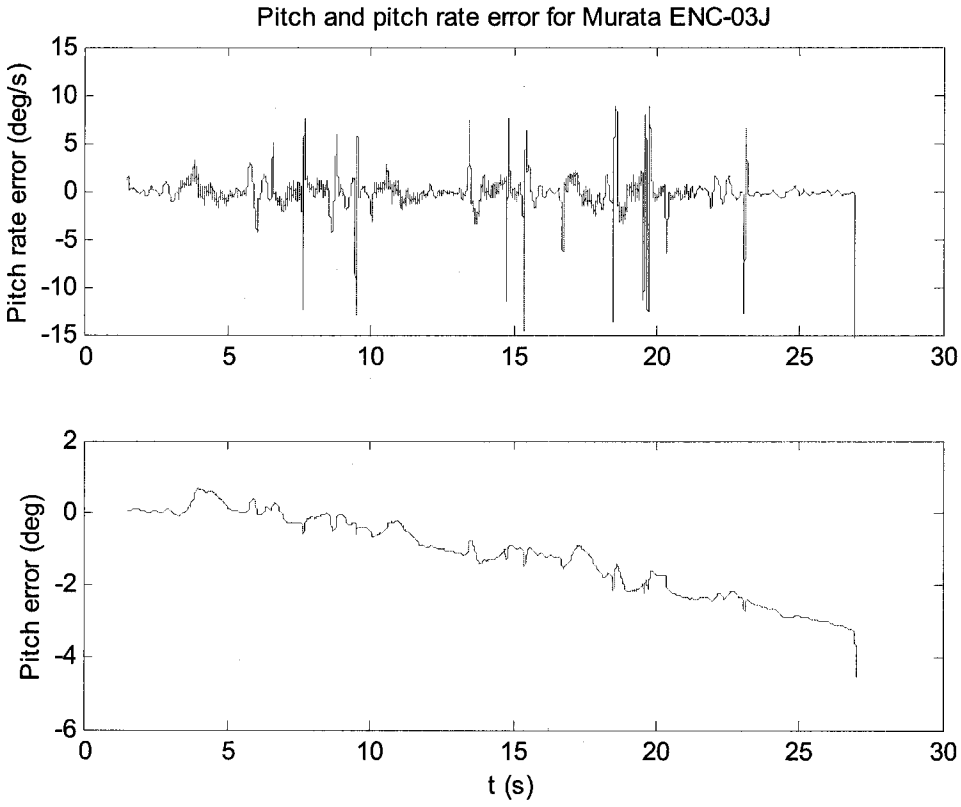

Figure 28: Pitch and pitch rate errors for Murata ENC-03J

Murata ENV-05H

Figure 29: Murata ENV-05F-03 Gyroscope

The Murata ENV-05H offers improved bias stability (9 deg/s max drift over temperature range), resolution (25 mV/(deg/s)) and linearity (0.5

% full-scale). This gyro is suitable for applications requiring integration because of its higher scale factor and repeatable bias rate. Indeed, Murata markets this product as a "support sensor for car navigation systems". Unfortunately, this sensor has a dynamic range of only +/- 60 deg/s, which is far too small to be applied in the robot. Also, its bandwidth is limited to between 7 and 10 Hz @ 90 deg phase shift, which is far too low for RHex's needs. (To use attitude information for real-time state-feedback control, bandwiths closer to 1000 Hz are preferred).

Interferometric Fibre-optic Gyros (iFOGs)

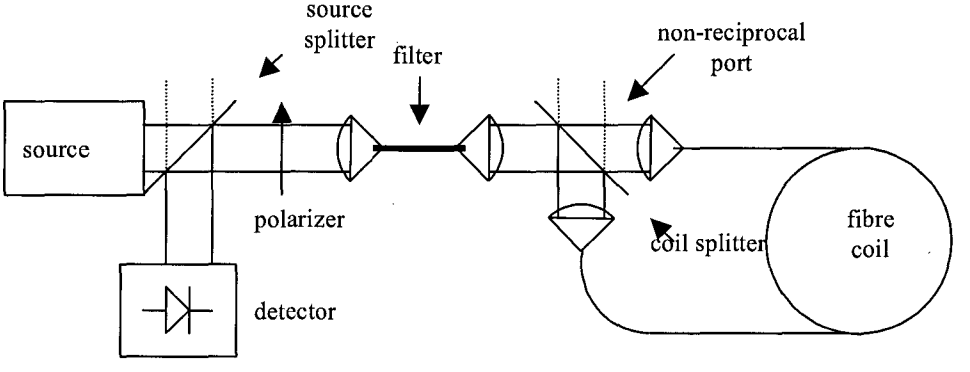

Figure 30: Block diagram of fibre-optic laser interferometer gyroscope (reproduced from [25])

Interferometric Fibre-optic Gyroscopes (iFOGs) operate by measuring the phase difference between two components of a polarized laser beam travelling in opposite directions around a polarization-preserving fibre optic coil [26]. The phase difference is called the Sagnac phase after Georges Sagnac, who first suggested similar experiments in 1913 demonstrating the existence of the ether [27]. This technology has recently resulted in substantial improvements in bias stability and drift for gyroscopes. Sagnac gyros are beginning to compete with

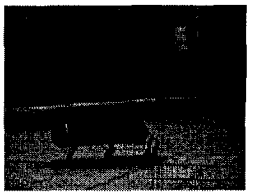

conventional mechanical gyros in aerospace applications due to their low drift and the high reliability associated with their solid-state design [28].

Sagnac-effect gyros have a major defect: they tend to produce an output that is strongly non-linear in rotation rate [29]. Fortunately, this nonlinearity is a repeatable function of rotation rate and temperature. Thus, with suitable testing, a fibre optic gyroscope may be considered as a replacement for a mechanical gyro. Many iFOG manufacturers, including Fizoptika and KVH, offer products which incorporate nonlinearity correction for maximum performance. However, at time of writing this feature was only available in models too large to install in RHex.

Fizoptika VG941 series

The Fizoptika VG941-3D was selected for evaluation for two reasons. First, to our knowledge this is the smallest commercially available three axis FOG (it was the only three axis FOG which would fit inside the robot's frame, along with existing components). Secondly, it offers adequate performance in all areas and excellent performance in many. In particular, dynamic range is +/- 500 deg/s, bias stability is < 0.03 deg/s at a fixed temperature. To get the required bias stability (discussed below) with this gyro, experiments were performed at fixed temperature. Manufacturer's specifications state that temperature-related drift can be compensated using a polynomial function of measured angular rate.

Technology Summary

Table 4 shows a comparison of four commercially available rate gyroscopes. While a large number of other gyroscopes are available, these are representative samples of two technologies considered: Interferometric Fibre Optic Gyros ("iFOG") and Coriolis effect vibrating prism gyros.

Based on some early experiments with the ENC-03J gyro during pronking, the following specifications were found to be required for accurate attitude estimation during pronking.

1. Maximum angular rate, bandwidth > 300 deg/s.
2. Must produce position estimates with < 3 deg error over 1 minute. This implies
    a. Good bias rate stability (< 0.05 deg/s error)
    b. Very low or compensatable scale factor non-linearity
3. Three axes are required (see following sections)
4. Must physically fit inside RHex allowing room for other components
5. Insensitivity to shocks and linear accelerations.
6. Weight should be as low as possible, not more than 1 kg.

Table 4: Comparison of some commercially available rate gyros. Inadequate performance specifications are highlighted. Data is based on pre-calibration tests.

Gyro Type		Coriolis		iFOG	
Gyro		ENC-03J [30]	ENV-05H [31]	E-Core RD2100 [32]	VG941-3D [33]
Input Range	°/s	300	80	100	500
Resolution (noise)	°/s	N/S*	0.1	0.004	0.002
Nonlinearity	% FS	5	0.5	0.5	10
Nonlinearity, OTR†	% FS	20	N/S	2	5
Bias rate stability	°/s	N/S	N/S	0.002	0.03
Bias rate stability, OTR	°/s	N/S	9	0.2	0.5
Bandwidth	Hz	50	7	100	1000
Update rate		N/A‡	N/A	100	279
Scale Factor	mV/(°/s)	0.67	22.2	20	4
Angle Random Walk	(°/hr)/√Hz	N/S	N/S	5	7.2
Mass	g	1	50	340	470
Power Consumption	W	0.025	0.085	3	4.5
Approx. Cost / Axis	US $	60	300	2500	1700

* N/S = Not Specified

† OTR = Over Temperature Range

‡ N/A = Not Applicable

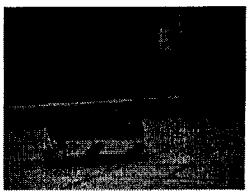

3.4 The Kinematic Problem

Why three gyros are better than one

Preliminary experiments with the Murata ENC-03J showed some very strange results. When the robot was constrained to rotate only in the plane of the gyroscope, reasonable pitch rate and pitch estimates were obtained over short periods of time. However, when the robot was placed on the floor and allowed to walk, gyro drift increased rapidly without bound. After some consideration it became obvious that the problem was a simple (and well known) kinematic one: the pitch angle of the robot with respect to the ground can be manipulated without rotating the robot around its pitch axis. To illustrate this, consider the following sequence of rigid body rotations:

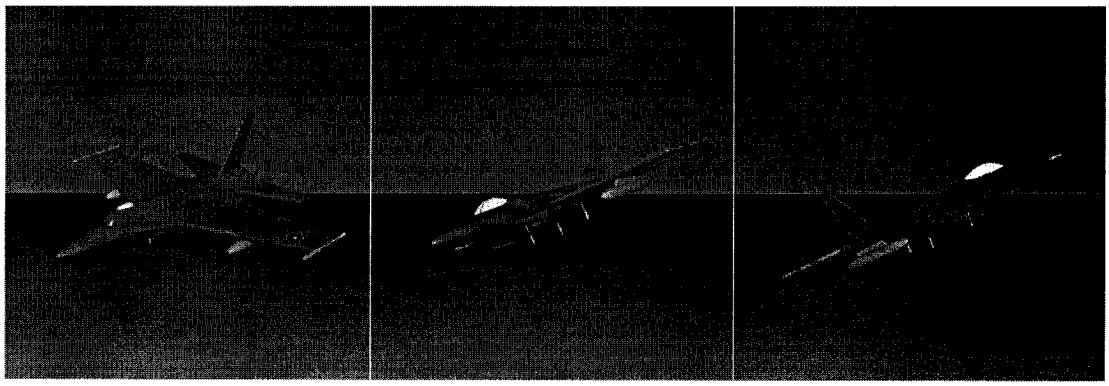

Figure 31: Sequence of rotations resulting in 45 degree pitch without rotation about the pitch axis. Step 1: vehicle rolls 45 degrees. Step 2: vehicle yaws -90 degrees. Final orientation is R: 0, P: 45, Y: 90.

This serves as a stern intuitive reminder of what is already known from basic kinematics: rotations are both non-separable and non-commutative. When the world-frame orientation is needed, all axes must be considered.

Selection of coordinate systems

In order to update a real time estimate of the attitude of the robot, the rate of rotation of the robot's coordinate frame with respect to some base frame must be expressed accurately. Gyroscopes such as those mounted in the robot are referred to as "strapdown" sensors because they measure the angular velocity vector of the robot with respect to its own moving reference frame. As a result, the angular velocity measured by strapdown sensors must be rotated into a base frame before being integrated.

Euler Angles

If one considers the evolution of a sequence of rotations in terms of their Euler angles, it is apparent that after every minute incremental change in orientation the Euler angles must be defined in a new coordinate frame. Euler angles, as a result, have no global properties which would permit the tracking of attitude under rotations [34]. Also, unambiguous interpretation of orientation from Euler angle representations is prevented by singularities at certain orientations (sometimes known as "gimbal lock" singularities).

To avoid these difficulties, a coordinate system that is singularity-free and allows easy transformation of angular rates from one frame to another must be chosen. Three commonly used choices present themselves: the direction cosine matrix; the axis-angle, or 'twist', representation; and 'quaternions', or Euler-Rodrigues parameters [35].

Direction Cosines

The direction cosine matrix, giving the exact coordinates of the unit vectors of the frame of interest in the base frame, is obviously an

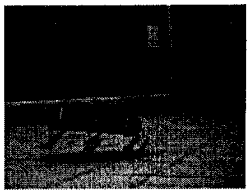

unambiguous form of representation. It lends itself naturally to calculation, as rotations of frames are simply matrix products. However, it is not a compact representation as only four parameters are required to represent orientation unambiguously [34] instead of the nine direction cosines.

Also, while direction cosine matrices lend themselves conveniently to the transformation of vectors such as the angular velocity vector from one reference frame to another, it should be noted that the integration of the angular velocity vector in base frame coordinates will not help us as the angular velocity vector is not the time derivative of a vector, and its integral does not correspond to an angular displacement [35].

Despite the non-compactness of the direction cosine representation, a solution for base frame attitude is given as follows. Note that the nonlinearity of this approach may have undesired effects on the integrator error growth.

Direction Cosine Kinematics and Integration

A relatively simple method of accumulating the world frame orientation of the robot is as follows. At the i^{th} time step, it is assumed that the rotation matrix can be approximated by a function of the RPY (roll, pitch, yaw) rates and the time step duration:

$$Q_i = Q_i(\dot{\phi}_{i-nav}, \Delta t_i) \qquad (14)$$

("nav" indicates the navigation, or "world" frame, whereas "body" indicates the robot frame)

We let $Q_{total,\,k} = Q_{next}$ (at k^{th} iteration) be the aggregate rotation matrix after k time steps, so that for every time step,

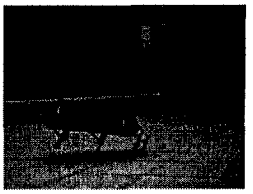

$$Q_{next} = Q_{incremental} Q_{last} . \quad (15)$$

Each incremental rotation matrix must represent the relative change during this time step in the navigation coordinate frame, as opposed to the body frame. This requires the vector of RPY rates in the world frame, which is approximated as $\dot{\vec{\phi}}_{nav} \approx Q_{last} \cdot \dot{\vec{\phi}}_{body}$. This last vector is simply the vector of rate outputs from the three gyroscopes on the robot.

Once the RPY rates are expressed in the navigation frame, the incremental rotation matrix is calculated as:

$$Q_{RPY} = \begin{bmatrix} c_\varphi c_\theta & c_\varphi s_\theta s_\psi - s_\varphi c_\psi & c_\varphi s_\theta s_\psi + s_\varphi s_\psi \\ s_\varphi c_\theta & s_\varphi s_\theta s_\psi + c_\varphi c_\psi & s_\varphi s_\theta c_\psi - c_\varphi s_\psi \\ -s_\theta & c_\theta s_\psi & c_\theta c_\psi \end{bmatrix} \quad (16)$$

where each angle is approximated as $\dot{\phi}_{i-nav} \cdot \Delta t$.

To summarize, the method for calculating the next rotation matrix in terms of the last is as follows:

1. $\dot{\vec{\phi}}_{i-nav} \approx Q_{last} \cdot \dot{\vec{\phi}}_{i-body}$
2. $\vec{\phi}_{i-nav} \approx \dot{\vec{\phi}}_{i-nav} \cdot \Delta t$
3. $Q_{i-incremental} = \begin{bmatrix} c_\varphi c_\theta & c_\varphi s_\theta s_\psi - s_\varphi c_\psi & c_\varphi s_\theta s_\psi + s_\varphi s_\psi \\ s_\varphi c_\theta & s_\varphi s_\theta s_\psi + c_\varphi c_\psi & s_\varphi s_\theta c_\psi - c_\varphi s_\psi \\ -s_\theta & c_\theta s_\psi & c_\theta c_\psi \end{bmatrix}$
4. $Q_{next} = Q_{i-incremental} Q_{last}$

Results

While this method produced correct estimates of attitude for periods of up to a minute a simpler approach requiring fewer approximations was

sought to ensure that the information given by the gyro was used in the best possible way. Thus, although this approach appeared to work, it was quickly discarded in favour of the far more elegant quaternion integration method.

Quaternion Kinematics and Integration

Obviously, the steps outlined above would be simplified greatly if the angular rotation rates measured by the gyros could be transformed directly into a rate that could be integrated in the base frame to obtain an estimate of attitude. This is in fact possible and is most easily achieved with the help of quaternion coordinates (also known as Euler-Rodrigues parameters). (The term "quaternion" could refer to any collection of four items, but usually refers specifically to the four parameter orthogonal group used to describe rotations by William Rowan Hamilton in 1843 [36]).

A quaternion is a four-tuple which can be used to represent the orientation of a rigid body in much the same way as axis-angle (or "twist") notation. In fact, a quaternion is constructed in a similar manner as a twist vector:

$$\mathrm{q} = \begin{bmatrix} q_1 \\ q_2 \\ q_3 \\ q_4 \end{bmatrix} = \begin{bmatrix} e_x \sin(\phi/2) \\ e_y \sin(\phi/2) \\ e_z \sin(\phi/2) \\ \cos(\phi/2) \end{bmatrix} \tag{17}$$

(e is the unit axis vector and ϕ is the angle of rotation about that axis in axis-angle coordinates)

However, there are two important differences between axis-angle notations and quaternion representations. First, notice that the

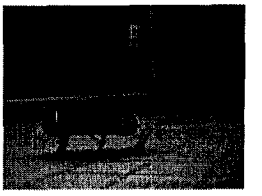

magnitude of the quaternion q = $|e| \sin^2\phi + \cos^2\phi = 1$. This means that quaternions take values in a unit sphere in $\Re^4$. Moreover, the multiplication of one quaternion with another (using the special quaternion product) rotates the first by the rotation specified by the second in much the same way that angles specified using $e^{j\theta}$ polar notation can be multiplied to produce rotations in two dimensions.

Thus in quaternion coordinates, the angular rate in the body frame may be translated directly into a world frame "quaternion rate" by multiplying it by a matrix constructed from the current attitude quaternion:

$$\dot{q} = \frac{dQ}{dt} = \frac{1}{2} Q \begin{bmatrix} \dot{R} \\ \dot{P} \\ \dot{Y} \end{bmatrix}, \text{ where} \tag{18}$$

$$Q = \begin{bmatrix} q_4 & -q_3 & q_2 \\ q_3 & q_4 & -q_1 \\ -q_2 & q_1 & q_4 \\ -q_1 & -q_2 & -q_3 \end{bmatrix}, \tag{19}$$

and each q_i is a component of current orientation quaternion. For the details of this derivation the reader is directed to [34].

This base-frame quaternion rate, $\dot{q}$, is the time derivative of the quaternion representing the orientation of the object of interest and may therefore be integrated to obtain the current estimate of attitude.

This is computationally simpler than the direction cosine integration both because no transcendental functions need ever be evaluated and

because the smaller dimension of the quaternion space means fewer multiplications need to be performed.

In evaluating the above equation numerically, the quaternion attitude estimate must be normalized after every integration time step to ensure that we stay within the space of quaternions (a unit sphere in $\mathbb{R}^4$). This is required to ensure that the rules of quaternion algebra are still applicable.

3.5 System Overview

The following block diagram shows the system used to estimate RHex's attitude.

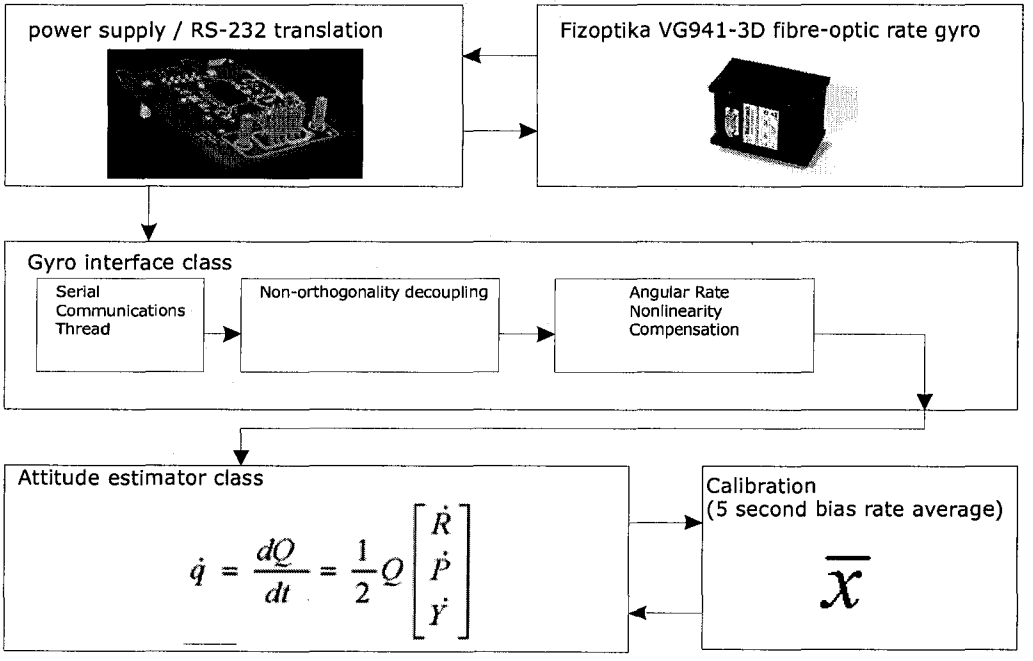

Figure 32: Gyroscope System Block Diagram

The sensor, a Fizoptika VG941-3D rate gyro is supplied with stable 5 V power by a power supply and RS-232/485 conversion circuit board. The rate gyro contains three Sagnac-effect coils, a 22 bit analog to digital converter (ADC) and a digital signal processor which drives the ADC and outputs serial data at 38400 baud via the RS-485 outputs.

The RHex computer accepts the RS-232 data from the interface board, and runs two C++ classes supported by the RHexLib library and realtime environment. The first class begins by correcting for the mutual non-orthogonality of the three axes using a decoupling matrix supplied by Fizoptika. Next, nonlinearity is removed from the decoupled angular rates by subtracting a polynomial function of angular rate, as described in the following section. The corrected and decoupled angular rate is then exposed in this class as the current angular rate vector.

Next, the attitude estimation class integrates the angular rate estimates provided by the gyro interface class using the quaternion integration method described above.
It is noteworthy that the Fizoptika VG941-3D comes with no internal power filtering and its outputs are therefore sensitive to variation in power supply voltage. Accordingly, a power supply board was designed to supply a clean, constant 5 V to the unit. For convenience, an RS-485/RS-232 converter was designed into the power supply board. The schematic for this combined unit is given in the appendix. The upper schematic block is an RS-485 to RS-232 level translator; the lower schematic block is a 5.0 V power supply supplying both the gyro and its level translator.

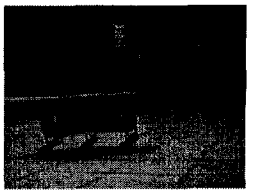

3.6 Gyro Nonlinearity Correction

Sagnac effect gyros produce an output that is a nonlinear function of the input angular rate (called the Sagnac phase) [37]. Error (the difference between the actual and reported angular velocity) may be accurately represented as a polynomial of at least degree three [38,39]. To obtain the coefficients of this polynomial, error as a function of reported angular rate was measured using a rotary stage equipped with a slip-ring, a quadrature encoder and approximate manual speed control [40].

Using the speed control, the speed was varied from roughly –500 degree/s to 500 degrees/s while time, the gyro outputs, the encoder position, and temperature (the gyro incorporates a temperature sensor) were recorded in a log file at a rate of 1000 samples/s. Apparatus for the experiment are shown in Figure 33. After each successful sweep, data was uploaded to a host computer and processed with a MATLAB™ script.

To obtain the polynomial error function, the following steps were performed:

1. Data pre-processing:
    a. Data were time shifted by 11 ms to provide strongest correlation between gyro rate and actual rate. (The source of the apparent 11 ms delay was not found)
    b. Data points near rapid changes in angular rate were removed.
    c. Data were low pass filtered with a Butterworth filter, f_c = 50 Hz.
2. Gyro rate error was fit as a degree-5 polynomial function of gyro rate, using the MATLAB™ function *polyfit*.

The resulting polynomial was later used to estimate correct the error from each gyro rate measurement.

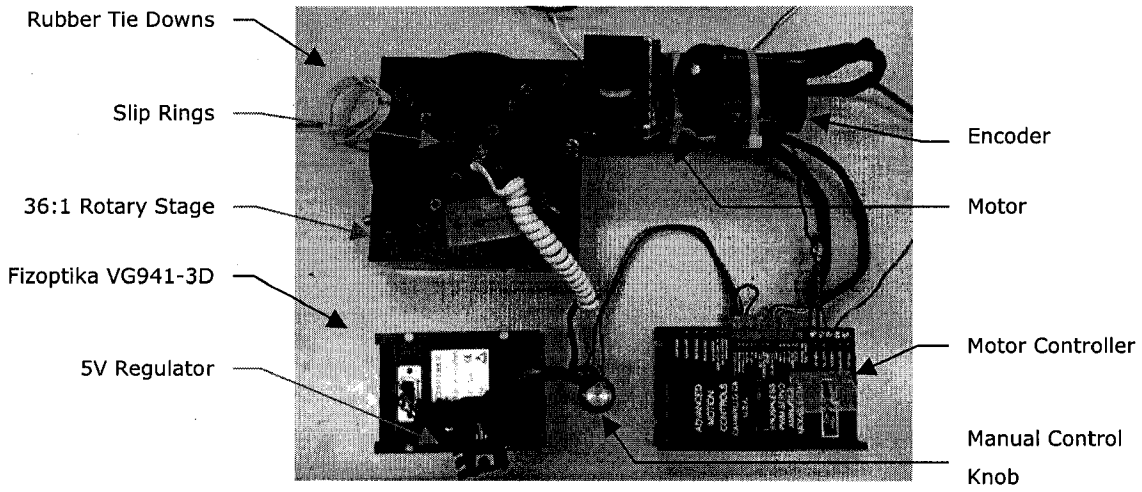

Figure 33: Aparatus for the measurement of scale factor nonlinearity

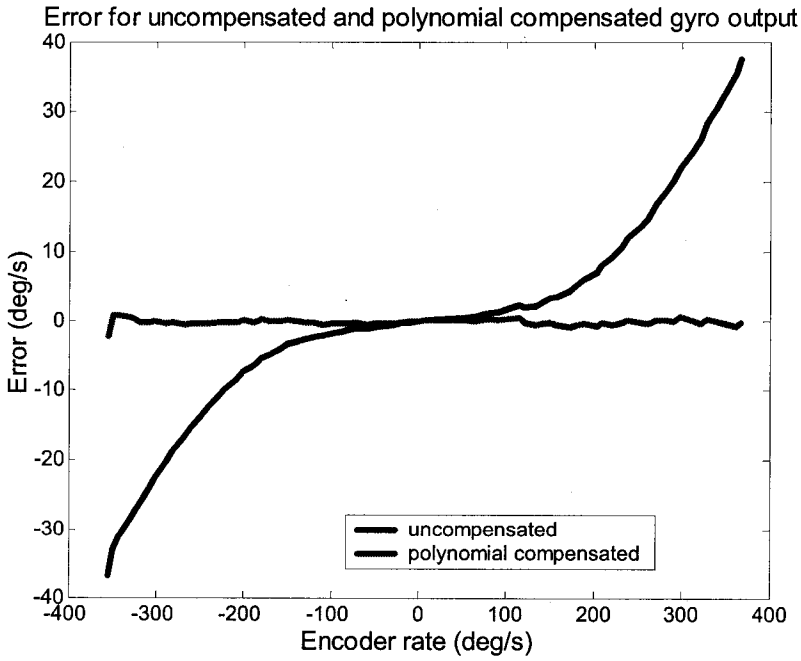

Figure 34: Angular rate error before and after polynomial compensation

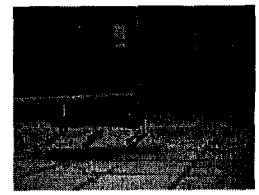

The improvement in performance made by polynomial compensation is partially illustrated in Figure 34, where the angular rate error is shown as a function of angular rate. A better illustration is to consider the impact of the angular rate error on the integrated estimate of rotation over time. If the gyro is rotated at 400 deg/s for one second, more than 40 degrees of error will be accumulated! Since accurate estimates of attitude are required for many minutes of operation, nonlinearity correction is essential to achieve reasonable performance.

3.7 System Performance

Performance specifications in inertial systems tend to involve a multitude of parameters, each having an impact on the performance under specific conditions. However, for pronking and other running gaits in RHex what really matters is the length of time for which one can expect that the estimate is valid within a specified precision. In the case or RHex, this specification set at a maximum of 3 degrees drift in one minute of pronking on flat ground at room temperature so as to enable short duration pronking experiments in the lab. Ideally, to validate the quality of attitude estimates, the robot's estimated orientation should be compared to that computed from a ground-truth measurement. However, as no system existed to provide ground truth measurements, only comparisons with known orientations could be performed periodically during trials.

Experimental results were taken from ten one-minute trials of pronking and one ten-minute trial. During each trial the robot would begin from a known orientation, pronk around the room for 60 seconds, and was then returned to its original orientation. Change in inertially-measured

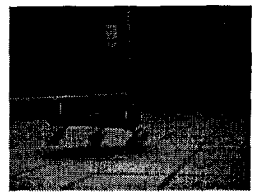

orientation on the yaw and pitch axes was recorded at the end of each trial. The mean and variance for the ten one-minute trials, as well as the one ten-minute trial, are displayed in Table 5. Adequate performance was obtained to allow control and sensing during short runs of pronking.

Table 5: Attitude estimator performance during pronking

Performance during pronking		
Trial duration	Pitch error (RMS °)	Yaw error (RMS °)
1	1.3	2.9
10	3.1	3.1

3.8 Future improvements

Future developments on RHex are likely to include extensions and modifications to this attitude estimate system that will both improve long-term accuracy and merge it with high-accuracy position estimates, resulting in full estimates of robot pose. The development path towards complete and reliable pose estimation is likely to include the following:

- Kalman filtering to improve gyro drift during integration
- Fusion of attitude estimation data with accelerometer data and possibly a magnetic heading sensor
- Temperature compensation of the Fizoptika VG941-3D gyro to provide accurate rotation estimates over all temperatures.

Chapter 4 Preliminary Model and Control of Pronking

Pronking, like every running gait, divides into two coupled dynamical systems: stance and flight. This chapter describes simple models for both stance and flight and a simple pronking controller based on these models which can make RHex run at up to 1.1 m/s.

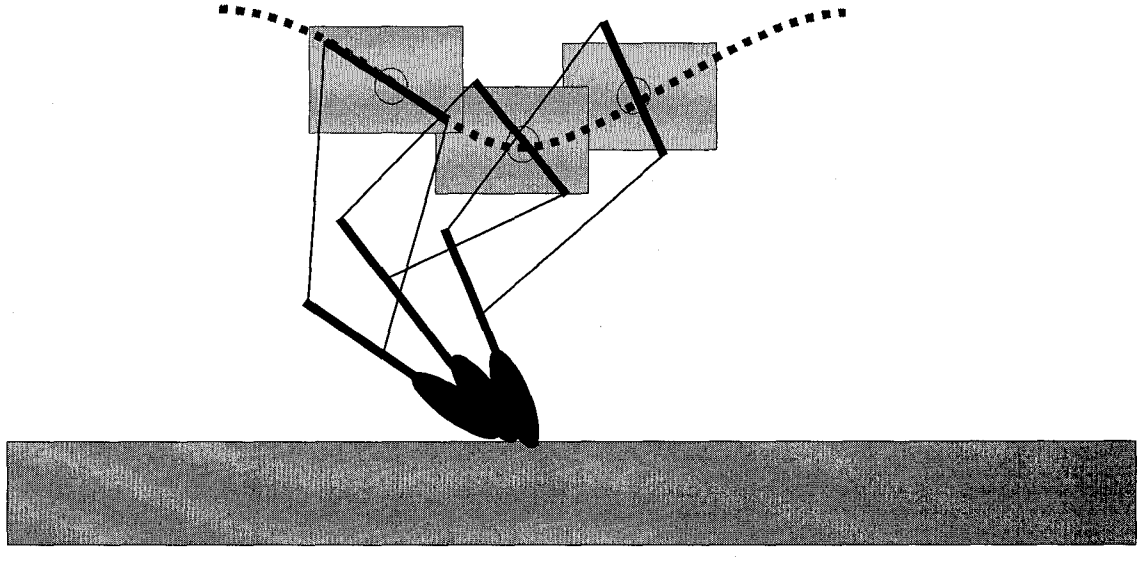

Figure 35: Spring-Loaded Inverted Pendulum (SLIP) model for running. Shown with RHex's characteristic four-bar springy legs.

4.1 Stance phase

The stance phase is defined as the portion of the gait during which leg contact with the ground prescribes the acceleration of the robot. As the robot lands with some initial downward velocity, the vertical dynamics for stance may be considered crudely as a spring mass oscillator. With this view, the time in contact with the ground should be one half the period of the spring mass system:

$$T_{\text{stance}} = \frac{1}{2}\frac{2\pi}{\omega_{\text{stance}}} = \pi\sqrt{\frac{m}{k}} = \pi\sqrt{\frac{8.0\,\text{kg}}{1900\,\text{N/m}\cdot 6}} = 83\,\text{ms} \qquad (20)$$

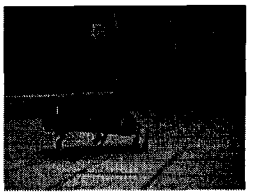

The robot's speed may be treated as approximately constant during stance, and equal to its overall average speed. In addition, if Raibert's touchdown angle is assumed to be a sufficient condition for stability, then the total angle subtended by the leg during stance may be calculated as follows (based on a forward speed of 1.0 m/s).

$$\theta_{td} = \arcsin(\frac{\dot{x}T_s}{2r}) = \arcsin(\frac{1.0\text{ m/s}\,(0.083\text{ s})}{2(0.14\text{ m})}) = 17.2° \quad (21)$$

$$\Delta\theta_{td} = 2\theta_{td} = 34.2°$$

There is an important constraint hidden in this equation: θ_{td} is limited to some range by toe-floor friction. As θ_{td} increases beyond this range, the robot will skid with each step, losing energy. As this constraint is difficult to model precisely, we assume a fixed maximum value of 25°.

Given this constraint, for every stance time (controlled by the robot's mass and leg stiffness) there must be a maximum speed. For RHex, with the above assumptions, this is:

$$\dot{x} \cong \frac{\Delta\theta_{s\,\tan ce} \cdot r}{T_{s\,\tan ce}} = \frac{50°(\frac{\pi}{180})(0.14\text{ m})}{0.083\text{ ms}} = 1.47\text{ m/s} \quad (22)$$

This calculation could be made much more precise with a simple model of the robot's toe friction and a kinematic model of leg force during stance. However, for our purposes it is sufficient to know that with a reasonable range of touchdown angles (up to about 25°) we may expect pronking at up to roughly 1.5 m/s.

This model excludes a great deal of relevant information, in particular the effect of touchdown impact and the horizontal and rotational dynamics of the robot during stance. On the other hand, this model is simple, useful and easily verified.

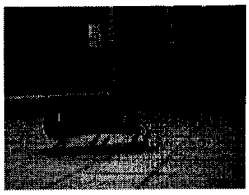

4.2 Flight phase

Flight phase is simply defined as the interval of time during which the acceleration of the robot's centre of mass is not due to leg-ground interactions. Thus with no ground forces acting (and therefore no non-conservative forces acting), we can safely postulate:

- horizontal velocity is preserved
- total energy is conserved
- total angular momentum is conserved
- the vertical motion is governed by the gravity-mass system with flight time given by:

$$T_{flight} = \sqrt{\frac{8h}{g}}, h \text{ is the apex height} \tag{23}$$

The flight phase model is rather more complete than the stance phase model. As no external forces are acting (except gravity, which is constant) we can be sure that the motion of the robot is completely specified by the above rules. A key result of the above postulates is that stimulation of this coupled oscillator, as well as control of other dynamic modes such as forward motion and rotations must be accomplished during stance.

4.3 Control Template

Careful consideration of the above equations leads one to wonder under what minimum conditions a forward running gait may be achieved. Raibert [41] showed in simulation that stable running could be achieved simply with the following ingredients:

- nominally passive (unactuated) stance
- touchdown detection
- leg retraction (swing) in flight to a the touchdown angle

- touchdown angle selected so as to esure a symmetrical stance phase
- control of body attitude during stance

This result was verified by the author in short sequences (3-5 consecutive hops) of stable hopping using a passive (ie. hip torque driven to zero) stance phase. To achieve stable passive hopping, the author commanded touchdown angles with respect to the horizontal plane. Some tuning was required initially to obtain stable behavior.

Based on Raibert's results a suitable control template for pronking must be able to do the following: (1) retract legs to touchdown angle during flight phase; (2) detect the transition from flight to touchdown; (3) stimulate vertical spring-mass oscillator during stance; and (4) detect the transition from stance to flight.

4.4 Materials and technologies required

In order to implement and test the pronking gait, the following was required.

- Gyroscopic measurement of robot pitch with respect to a world reference frame
- Adequate computational power to perform control calculations within a 1 kHz real-time control loop
- Adequate actuator power to stimulate the vertical spring mass system, as well as to influence other dynamical modes during stance
- Springy, resilient legs with spring stiffness in a specified range
- Mechanism for the detection of touchdown
- Software for real time leg trajectory tracking using conventional proportional-derivative (PD) control, with selectable gains

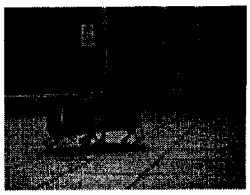

The substantial development effort required to produce the experimental apparatus mentioned above was made entirely by students working on the RHex project, including the author. The author is obviously indebted to his colleagues for this work, as reflected in the acknowledgements.

4.5 Preliminary Control

Touchdown detection state machine

Touchdown detection is performed based on the premise that the torques required to servo the legs during the interval prior to stance (when they are unloaded) are much smaller than those required after the beginning of stance. The leg-touchdown detection state machine takes as its input the motor current of each leg over time, and switches according to the state chart:

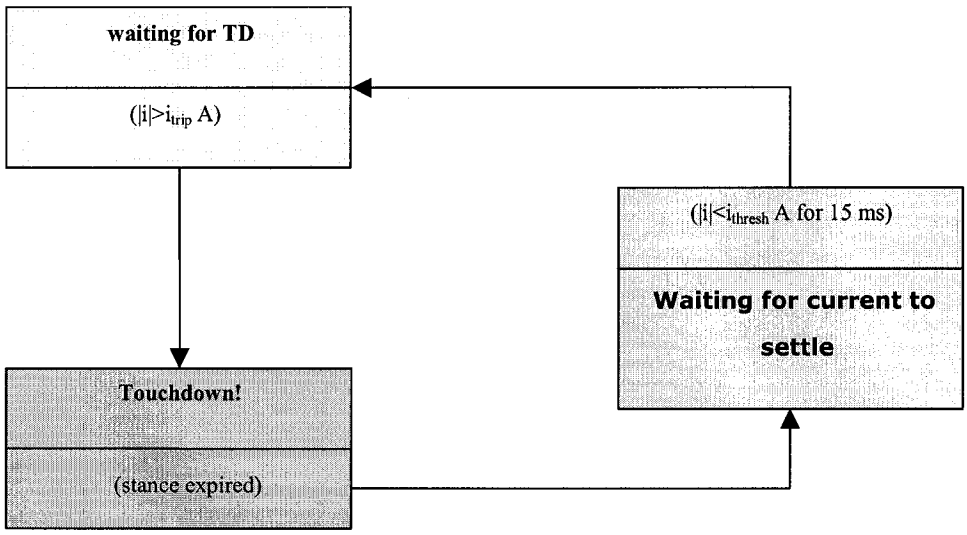

Figure 36: Touchdown detection state machine

An important part of the stance detection was accurate estimation of the motor currents. The simple model used for this purpose is described in the chapter on Motor Modeling and Current Estimation.

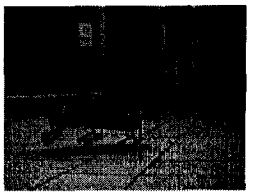

Performance of the touchdown detection was tested qualitatively by tapping a leg with a finger and tweaking the current thresholds for maximum sensitivity and minimum self-triggering. Quantitatively, a useful measure of performance for a touchdown sensor would be the degree to which the robot's state has been perturbed by touchdown before the sensor trips. In this case, maximum useful sensitivity of this touchdown detector was limited by its tendency to self-trigger, so quantitative optimization was not required.

Flight phase: leg retraction

Flight phase returns the legs to their required touchdown angles as fast as possible and without stubbing toes on the ground. If the legs could be moved arbitrarily quickly, then one would choose to move at a particular speed to minimise the probably of leg-ground interaction. In this case, however, minimum retraction times were long (typically >70 ms) in comparison to the flight times (typically ~100 ms) so the author sought to minimise the return time for the legs.

Careful tuning of flight phase gains was required to minimise retraction time while also ensuring rapid settling of motor currents (required to enable sensitive touchdown detection.

In Figure 37 retraction phase occurs between 10.26 s and 10.35 s. Controller gains are selected such that the leg settles to low torque output rapidly.

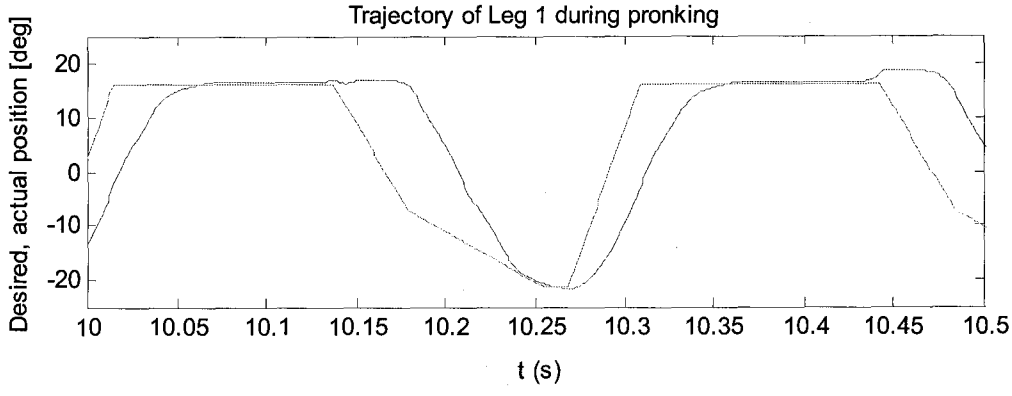

Figure 37: Front left leg trajectory through one complete hop. Protraction phase occurs between 10.13 s and 10.26 s

Stance phase: Protraction

The protraction phase serves two purposes during pronking. First, the protraction phase, coinciding with stance, is the only opportunity to add energy to the vertical spring-mass system and thus maintain hopping height. Second, this phase is the only time during which the robot may exert force to control its stability. It is also worthy of note that since the robot is only in contact with the ground during stance, nearly all of the power consumed in maintaining this gait is applied during protraction. Trajectory selection and tuning of the protraction phase is therefore essential to the stability, hopping height and efficiency of the gait.

In this simple open loop controller, protraction torques exerted during stance both propel the robot forward and cause it to pitch backwards (nose up). To reduce the backward pitching effect, a two-speed stance was selected with the speed of the first stance phase greater than that of the second phase. The desired effect was to compensate for the

backward pitching torque by slowing leg sweep while the robot was moving forward:

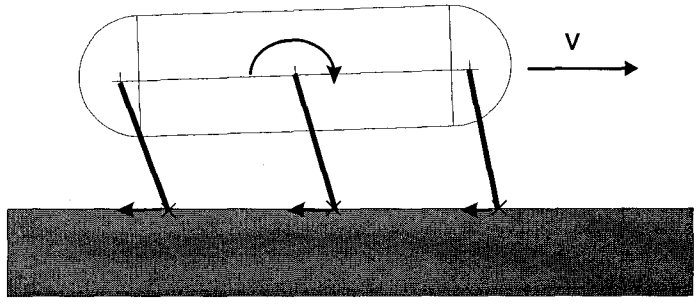

Figure 38: Illustration of effect of slow stance phase II

Combined controller

The state machine for the combined pronking controller is simply the union of the stance and flight phases, as shown in Figure 39.

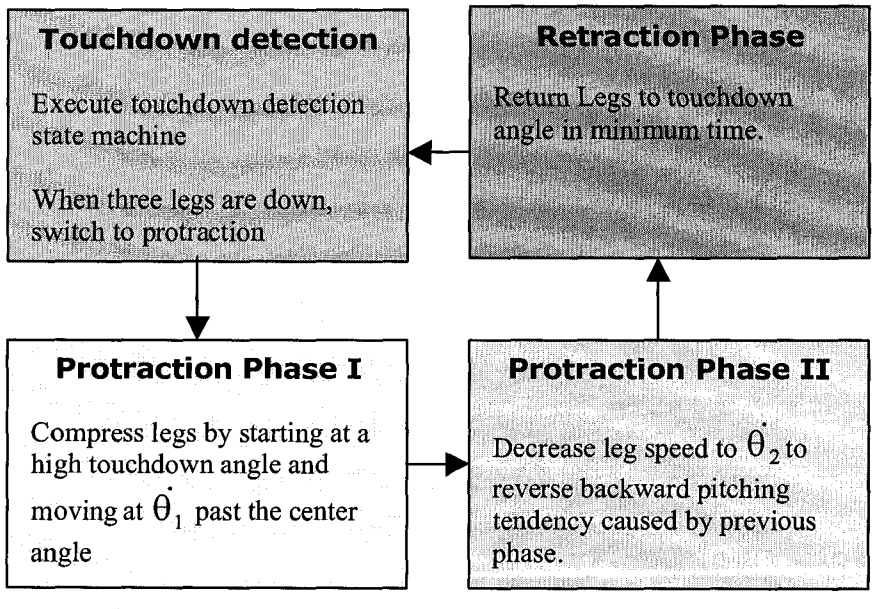

Figure 39: State diagram for basic pronking controller

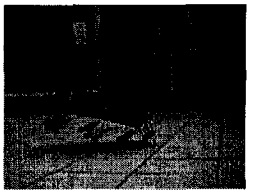

A typical leg trajectory generated by this controller during pronking is shown in Figure 40 together with shaded vertical bars indicating the controller state.

4.6 Experimental Results

Speed trials

Using only this simple clock-based gait and the crude touchdown synchronization provided by the touchdown detection state machine, experimental trials were conducted to evaluate the resulting efficiency and usability of this gait [42,43].

For each trial, RHex pronked across two lines marked 2 m apart on the lab floor. Using the robot's onboard measurement and logging system battery voltage and current, leg position and other variables were logged. Successful trials were defined as those during which the robot pronked without visible toe stubbing, tipping, or other instability. For each data set, trials were run until 20 successful runs had been logged. Table 6 shows the results of the twenty successful trials in this test bed. Twenty-five runs were performed in total, of which twenty were successful. Each elapsed-time measurement was taken manually, using a button on RHex's remote control and RHex's internal timing. Average speed, power and specific resistance for this data set were 0.97 m/s, 140 W and 1.85 respectively. A discussion of the definition and role of specific resistance, ε, will be presented later in the section "Speed & Energetics".

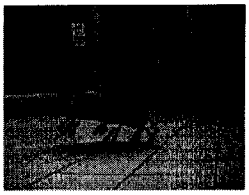

Table 6: Results for 20 trials of pronking on linoleum

Elapsed Time (s)	Mean speed (m/s)	Mean Power (W)	Distance (m)	ε
1.9167	1.0435	138.3164	2	1.6980
1.8167	1.1009	138.3788	2	1.6102
1.8567	1.0772	140.1852	2	1.6671
1.9367	1.0327	136.0177	2	1.6873
1.9367	1.0327	144.7217	2	1.7953
2.0756	0.96356	137.2807	2	1.8251
2.1377	0.93558	144.2262	2	1.9748
2.0767	0.96308	135.3704	2	1.8006
1.9967	1.0017	142.0365	2	1.8165
2.3166	0.86333	139.3939	2	2.0684
1.9967	1.0017	143.4055	2	1.8340
2.2566	0.88627	143.0252	2	2.0673
2.3356	0.85631	145.4501	2	2.1760
2.4367	0.82078	140.3951	2	2.1912
1.9367	1.0327	131.0635	2	1.6258

The gait parameters for these trials are shown in Table 7. The front four legs (legs 1,2,4,5) used one set of parameters while the back two used another. Parameters were chosen to maximize success rate and speed while minimizing power consumption. This required tuning for very low ground clearance during flight so that the back legs were dragging, or nearly dragging, during stance.

Table 7: Gait parameters for speed trials

Legs		Parameters				
		θ_{td}	$\theta_{dot\ 1}$	$\theta_{dot\ 2}$	α	t_{swp}
	Front 4	18	560	180	0.33	0.130
	Back 2	15	480	180		

4.7 Typical leg trajectory plot (trial 2, leg 1)

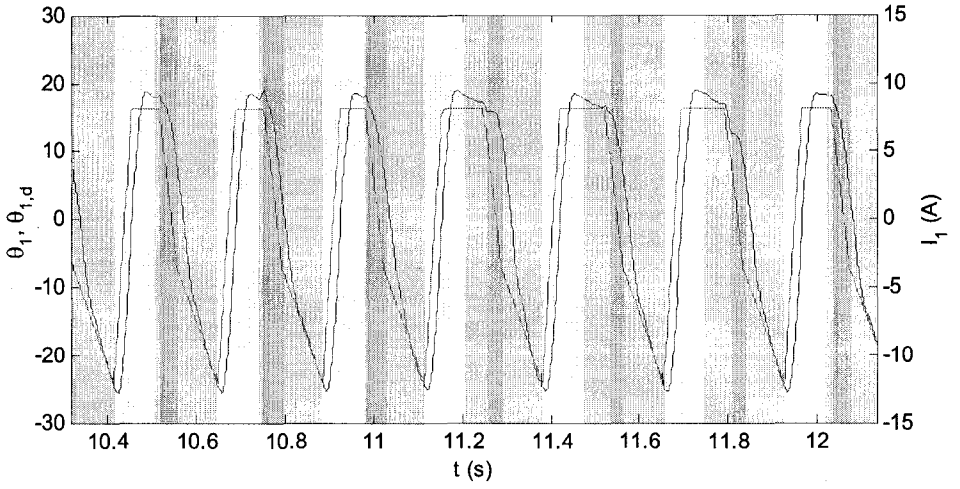

Figure 40: Leg trajectory (leg 1) during 2 m pronking trial.

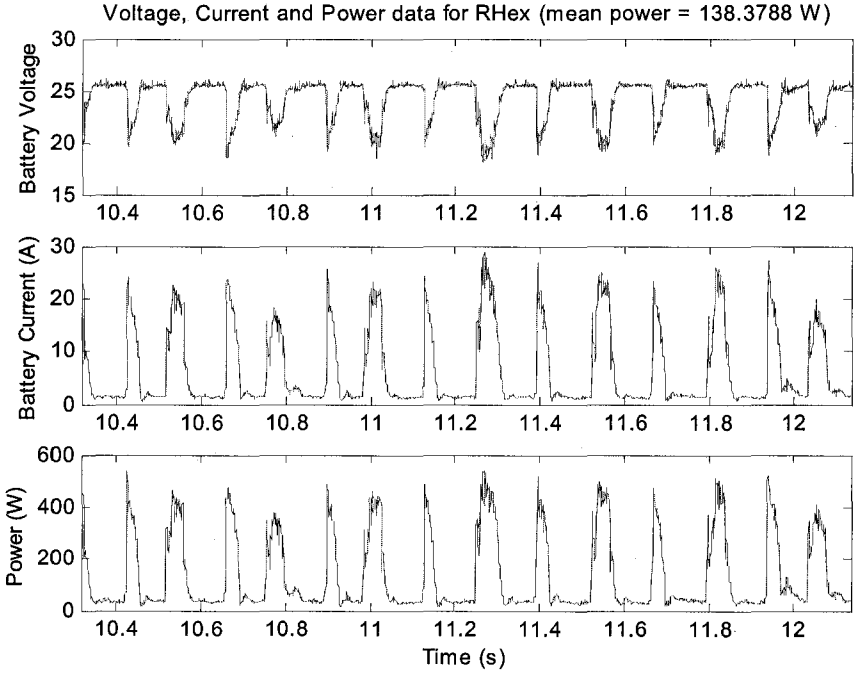

Figure 41: Power consumption during 2 m pronking trial. A model for battery voltage as a function of current ($V = V_o - IR$) is overlayed on the voltage data (V_o=25.9 V, R = 0.267 Ohms) for comparison. The model data are nearly indistinguishable from the voltage trace.

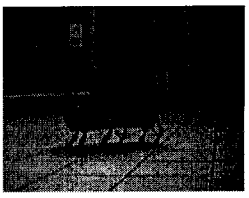

Model Validation

Figure 42 shows the orbit of vertical position versus velocity. Such plots can be used to examine a 2-D cross-section of the state space of a dynamical system. Stable periodic motion, such as in running, results in closed periodic orbits.

Though the data are too noisy to permit quantitative conclusions, the distinct shapes of the stance and flight phases tell us that the model for pronking is qualitatively correct. Flight phase is distinctly parabolic, verifying what must certainly be true: the centre of mass is following a simple ballistic trajectory under the influence of gravity. During stance phase a harmonic (ie. elliptical) trajectory is observed, consistent with the simple spring-mass oscillator hypothesis.

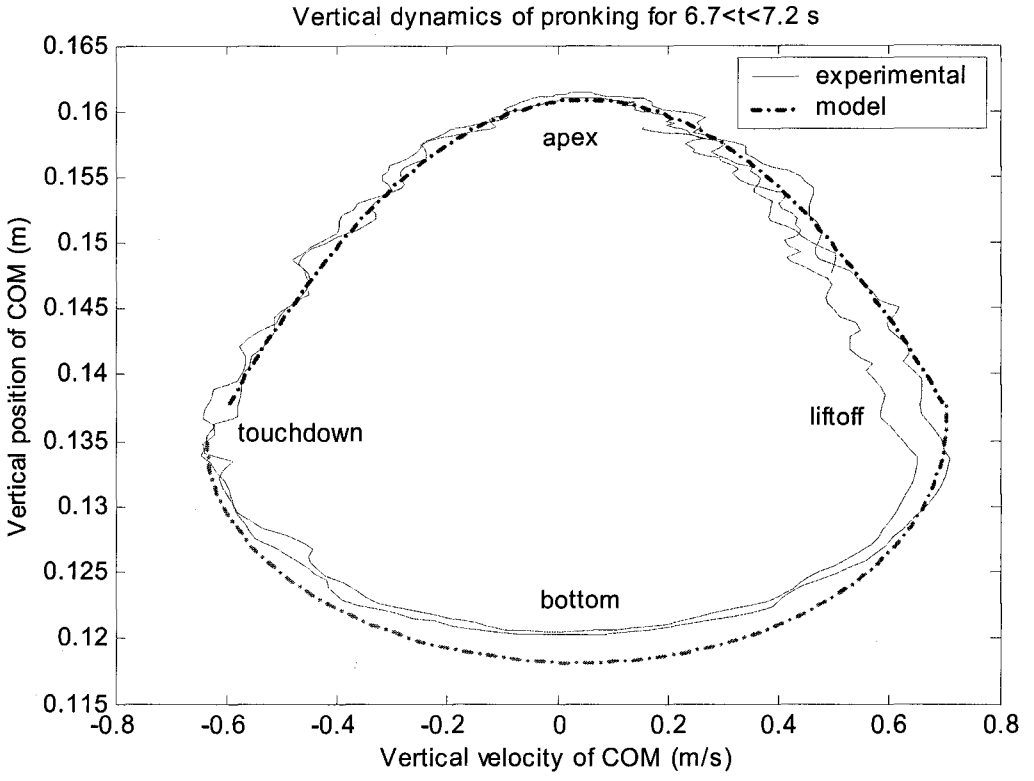

Figure 42: Orbit of vertical position / velocity during pronking. Data double integrated (with constants selected to match stance phases) from accelerometer data.

As stance time is a particularly important parameter for this model it was verified separately in a sequence of ten drop-test experiments. For each experiment, the robot was dropped from a short height above the ground and video was captured at 1000 frames per second.

Table 8 shows the results for each drop test trial. The mean for the experiment was 85.1 ms and the standard deviation was 3.5 ms. Touchdown and takeoff times were measured visually using the 1 ms timer integrated with the high-speed video camera.

Table 8: Results of stance-time drop test trials

Trial	Touchdown (ms)	liftoff (ms)	stance time (ms)
1	297	380	83
2	399	493	94
3	148	230	82
4	203	287	84
5	231	319	88
6	214	300	86
7	192	276	84
8	233	316	83
9	411	494	83
10	154	238	84

Multi-surface trials

Besides the linoleum used to perform the speed and energetics trials, the basic (open-loop) pronking controller was also tested on three other surfaces: carpet, tile and snow-covered paving stones.

Though energetic measurements were not performed, the following qualitative observations were made. On carpet the robot pronked with greater ground clearance, less stability and lower speed. Runs were frequently punctuated by flips. On tile the performance was qualitatively similar to linoleum; long sequences of stable fast hopping were observed. On snowy concrete the robot more or less dragged its legs, occasionally halting as it dug into the snow.

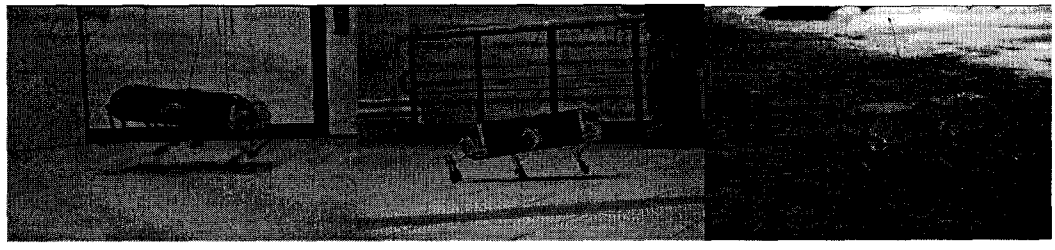

Figure 43: Multi-surface trials

4.8 Discussion

Speed & Energetics

Energy efficiency strongly affects the robot's run time and is a key performance parameter for any autonomous mobile robot. Figure 44 compares RHex pronking and walking energetic performance, based on the "specific resistance" or energy cost of locomotion per unit distance. Specific resistance is defined by the following equation,

$$\varepsilon = \frac{P}{mgv},$$

where P is the average power consumed, m is the mass of the robot, g is the acceleration of gravity, 9.8062 m/s^2, and v is the average velocity of the robot. This measure is extremely useful in the comparison of vehicles (both legged and otherwise) because it is normalised by the weight of the vehicle, and thus allows meaningful comparisons to be made between large and small vehicles. Specific resistance may be defined in terms of the total or net power (ie. power used to locomote only versus total power consumption) and in terms of either total robot mass or payload mass [44]. In RHex's case we use the average electrical power consumed from the batteries, based on real-time measurements of voltage and current from RHex's batteries, and the

total mass of the robot. Speed is calculated based on the time taken to move from the starting line to the finish line, and the length of the trial.

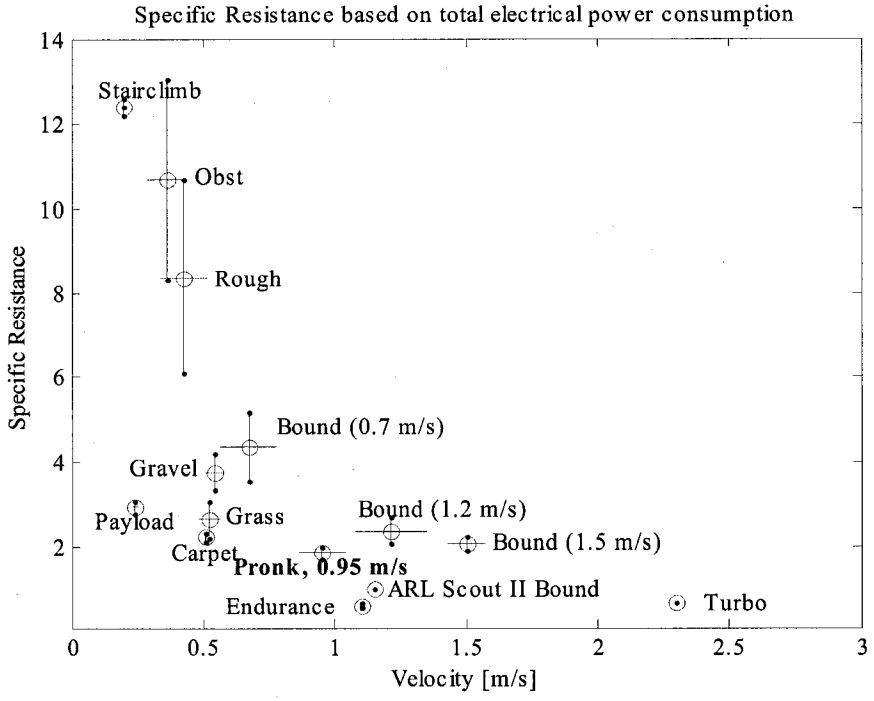

Figure 44: Energetics of RHex for various gaits and terrains

Summary of experimental results

The basic open-loop pronking gait resulted in a substantial improvement both in speed and efficiency of locomotion over RHex's initial walking gait. Though recent developments have resulted in even faster and more efficient running gaits for RHex, the pronk is still one of two gaits (hi-speed tripod run [a.k.a. turbo mode] being the other) on RHex to achieve a specific resistance less than 2.0.

Despite this, the gait had several limitations in terms of usability. First, the success rate in the controlled environment of 2 m trials on linoleum was limited to around 80 %. Outdoors and on carpet and other

surfaces, pronking was consistent only for short runs of five to ten consecutive hops. These runs tended to end in one of two ways: (1) loss of clearance necessary to avoid toe stubbing, and (2) nose dives caused by large downward pitch rate resulting from premature touchdown of the hind legs.

Though the motivation for a springy legged running gait is clear from the energetic results, such a gait must be robust and reliable on at least flat terrains such as asphalt and linoleum before it will be of substantial benefit to RHex.

4.9 Simulation of Basic Pronking

To validate the understanding gained from experimental work on pronking in RHex, a Working Model 2D™ sagittal-plane dynamic simulation was written using a physically realistic model of RHex and a similar gait controller. Similar performance to the real robot's speed was observed in simulation, though power consumption in simulation was higher (gains were not tuned to minimize power consumption).

Model Description

Simulation provides a sterile, controlled environment in which to study the dynamics of locomotion. As the robot already pronked when this simulation was written, the goal in writing this simulation was primarily to determine if any factors had been overlooked which helped the robot to pronk without the author's knowledge.

Model Parameters

Accordingly, the simulation was kept as realistic as possible to the extent of available knowledge about the physical parameters of the robot. Key parameters are listed in Table 9.

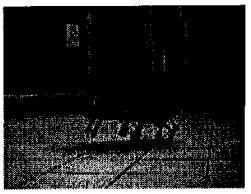

Table 9: Simulation Parameters

Parameter	Value	Unit
Leg stiffness	1879	N/m
Leg damping	16.28	N/(m/s)
Body Mass	7.6	kg
Body Inertia	0.171	$kg \cdot m^2$
Length	0.4	m
Leg Mass	0.076	kg
Leg Length	0.14	m
Motor max torque at hip	6.3	N·m
Motor max speed at hip	31.76	rad/s
Battery voltage	24.0	V
Acceleration of gravity	9.8062	m/s^2

Simulation results

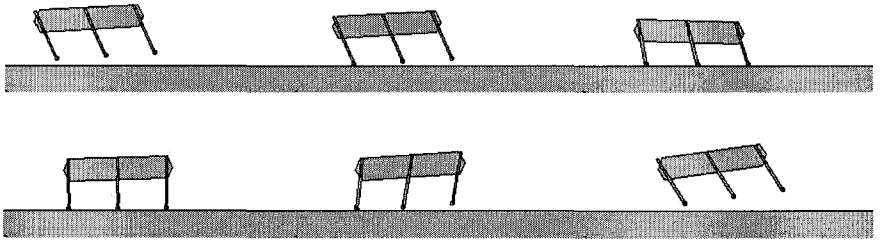

Vertical dynamics

Interestingly, the vertical position / velocity orbital is different in simulation than the one obtained for pronking in the real robot. Although the basic shape of ballistic flight and harmonic stance are shown clearly in the simulated data, equally clear are two strong deviations from this model. For a sagittal plane quadruped model, Jeff Koechling [45] attributed a notch just past takeoff to the expanding legs

hitting end of travel. Though this notch is absent from Figure 45, we note a deviation from ballistic motion after takeoff; position increases sharply roughly halfway between takeoff and flight. This may be explained in terms of two forces that act between the robot and its legs during retraction:

- Centripetal force as legs are moving, $F_c=mv^2/r$
- Inertial force for acceleration and barking of leg through flight trajectory, $F_I=\tau r_{cl}\sin(\theta)$

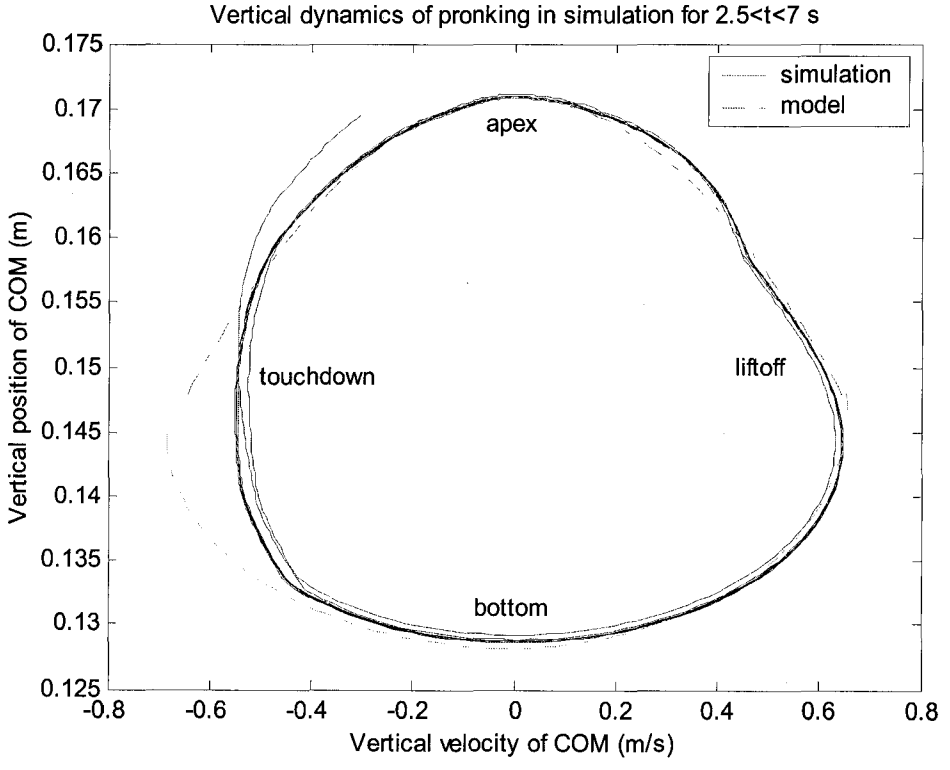

Figure 45: Orbital plot of vertical position vs velocity for pronking in simulation

Another key difference between Figure 45 and the phase plots shown by Koechling [45] and Raibert [41] is the protracted period of constant

velocity near −0.57 m/s. This effect may be explained by the transfer of vertical potential energy to rotational kinetic energy as the robot pivots around the back toe (which always touches down early in simulation). It is perhaps worthy of note that this period of constant velocity does not appear on the orbital plot for the experimental run presented in Figure 42. This is explained simply by the fact that during the experimental pronking runs, early touchdown of the hind legs was less pronounced than during the simulated runs.

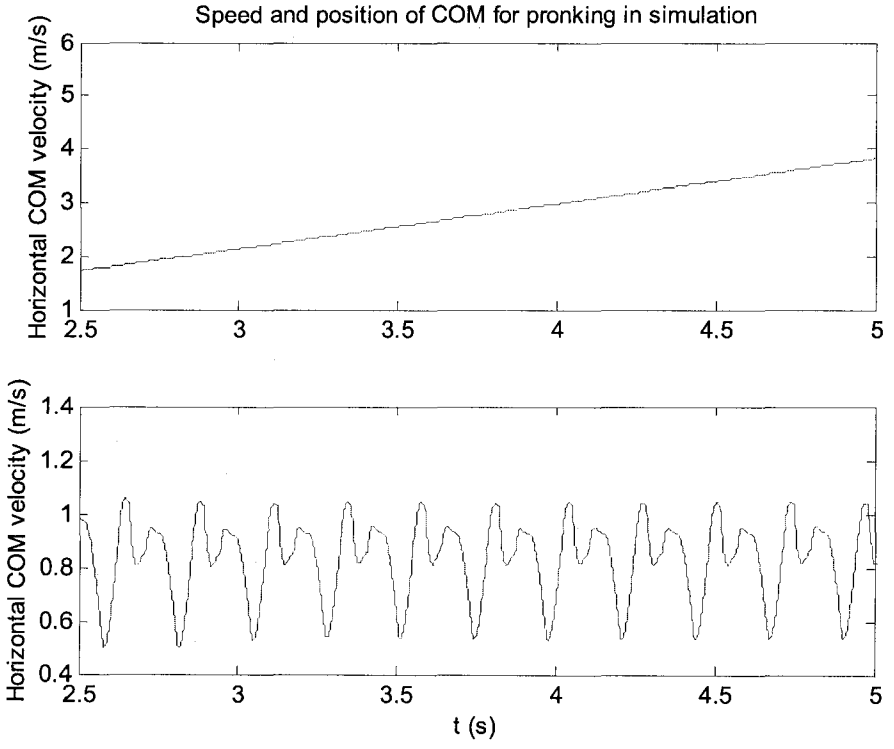

Figure 46: Horizontal position and speed during simulated pronking

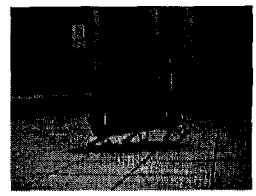

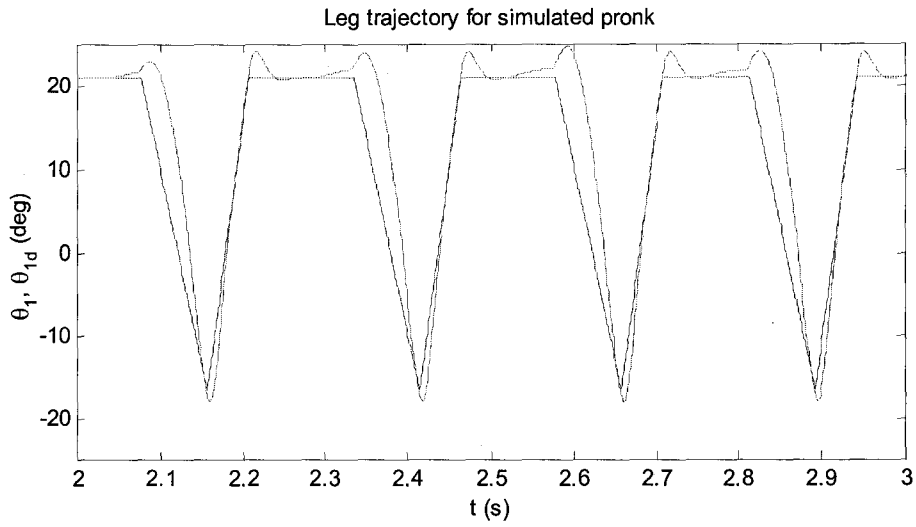

Figure 47: Typical leg trajectory (leg 1) during pronking

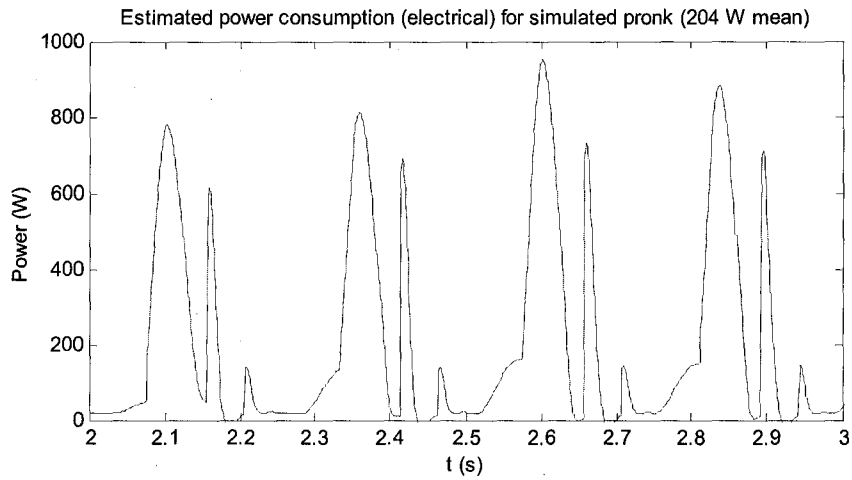

Figure 48: Electrical power consumption during simulated pronking

4.10 Conclusions and projected improvements

The experimental and simulated results presented in this chapter confirm the hypothesis that dynamic running gaits can dramatically improve the locomotion efficiency of RHex. However, this improvement

in efficiency is for the time being at the cost of the stability and usability of the robot, as the open-loop pronking gait is not sufficiently stable to provide reliable locomotion. During experimental trials, stable repeatable motion was obtained only for short periods of time over consistent surfaces. It is therefore likely that to improve the robustness of this controller the gait must be able to compensate for a wider range of disturbances both in the robot's motion and in the ground surface.

Of the unsuccessful experimental trials, a great number ended with the robot placing its feet too far behind and falling over forward. This, together with Raibert's insights into the balance of monopod robots, points to the need for a precise, speed controlled touchdown algorithm. Such an algorithm would rely on knowledge of both forward speed and robot attitude to select a touchdown angle resulting in stable hopping. As forward speed information is not yet available on RHex, the author sought to measure and control robot pitch alone as the solution to this problem. This is the subject of the following chapter.

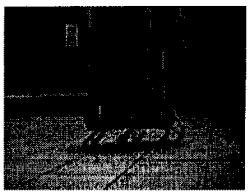

Chapter 5 Pitch Control During Pronking

5.1 Introduction and Motivation

A key result of the early investigation of open-loop pronking (ie. no online feedback) is that robot pitch and pitch rate are important parameters for stability. Due to the singular nature of the kinematics of RHex's six parallel actuator axes, no obvious direct input for the control of pitch is available. This chapter presents the study of two empirical methods for the control of pitch, based on the robot's interaction with the ground during stance: *kinematic pitch control* and *touchdown plane angle control*.

5.2 Inputs and Interactions

With a four-rigid-link sagittal plane model, RHex is singular with respect to pitch during stance when all legs are parallel and point downwards (zero leg angle). That is to say that hip torques applied with respect to the body result only in translational forces acting upon the body—they will have no influence over the pitch or pitch rate of the robot. Ideally RHex will be in the vicinity of this posture during a small duration of the stance phase. However, at other points during the stance phase we may be able to influence the pitch of the robot by applying different hip torques in different pairs of legs.

Worthy of note is the possibility of control of pitch during flight. We assume that the total angular and horizontal linear momentum are conserved during flight. Thus, by counter-rotating legs by multiples of full revolutions it should be possible to obtain discrete changes in robot

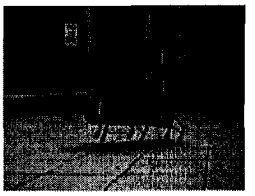

pitch. This method is not studied here because it would constrain the motion of the legs during flight in an awkward way.

Another key to the control of pitch is very likely the touchdown posture of the robot with respect to ground. Due to the large momentum of the robot just prior to touchdown, when speed is maximum, slight asymmetries in the toe touchdown times may have a strong effect on the robot's pitch during stance.

As explicit derivation of the equations of motion during stance is not the subject of this work, the hypotheses put forward here are heuristic—they are not a substitute for analytic or complete numerical solutions to the inverse dynamics problem. However, if they result in useable relationships between control inputs and the desired state variables, this approach will be justified.

5.3 Two hypotheses for pitch control

Kinematic Pitch control

A simple and well-used method for obtaining and exploiting control relationships in a robotic system is the kinematic equality [46,35]:

$$\tau = \mathrm{J}^{\mathrm{T}}\mathrm{F}\,, \tag{24}$$

where τ is the required actuator input (either force or torque), J^{T} is the transpose of the Jacobian matrix relating the joint rates to the end effector rates and F is the desired end effector force or torque*. This relationship connects in an exact and convenient manner the effect of

---

* This equation is often known as the Principle of Virtual Work, having derived originally from work done by Jean Le Rond d'Alembert.

actuator output torques with forces or torques at specific locations in a model. For legged machines, this method was perhaps first successfully used by Raibert in the control of "virtual legs" in a quadruped running machine [47].

In RHex, this equation may be used to give an approximate relationship between a desired pitch moment to desired hip motor torques for the purpose of regulating robot pitch.

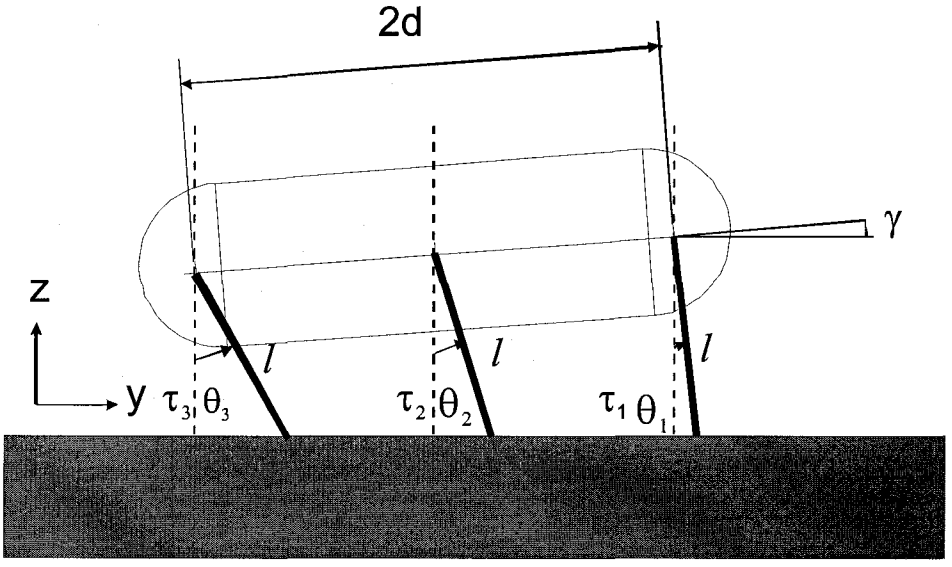

Figure 49: model of planar kinematics during stance used for calculation of pitch correction torques

In the derivation that follows, the effect of the middle leg torque on the pitch is ignored for two reasons. First, the equation for pitch is overdetermined when all three legs are considered. Second, the fore and hind legs are able to exert greater leverage over pitch due to their larger distance from the centre of mass. Thus neglecting the effect of the middle leg and assuming constant length legs, we write the configuration of the robot body in this planar model:

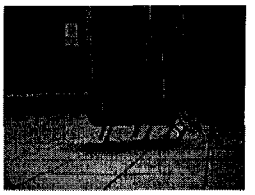

$$z_{com} = \frac{l\cos\theta_1 + l\cos\theta_2 + l\cos\theta_3}{3} \tag{25}$$

$$y_{com} = \frac{-(l\sin\theta_1 + l\sin\theta_2 + l\sin\theta_3)}{3}$$

$$\sin\gamma = \frac{l\cos\theta_1 - l\cos\theta_3}{2d} \tag{26}$$

$$\dot{z}_{com} = \frac{-(l\sin\theta_1\dot{\theta}_1 + l\sin\theta_2\dot{\theta}_2 + l\sin\theta_3\dot{\theta}_3)}{3} \approx \frac{-(l\theta_1\dot{\theta}_1 + l\theta_2\dot{\theta}_2 + l\theta_3\dot{\theta}_3)}{3} \tag{27}$$

$$\dot{y}_{com} = \frac{-(l\cos\theta_1\dot{\theta}_1 + l\cos\theta_2\dot{\theta}_2 + l\cos\theta_3\dot{\theta}_3)}{3} \approx \frac{-(l\dot{\theta}_1 + l\dot{\theta}_2 + l\dot{\theta}_3)}{3}$$

$$\cos\gamma\dot{\gamma} \approx \frac{l\sin\theta_3\dot{\theta}_3 - l\sin\theta_1\dot{\theta}_1}{2d} \tag{28}$$

$$\dot{\gamma} \approx \frac{l\theta_3\dot{\theta}_3 - l\theta_1\dot{\theta}_1}{2d}$$

Small angle approximations for sin() and cos() are applied to facilitate derivation since leg angles during stance are typically < 20 degrees.

By taking the partial derivatives of the configuration rates with respect to the joint rates, we obtain the Jacobian matrix relating hip torque to body pitch moment:

$$J = \begin{bmatrix} \frac{\partial\dot{y}}{\partial\dot{\theta}_1} & \frac{\partial\dot{y}}{\partial\dot{\theta}_2} & \frac{\partial\dot{y}}{\partial\dot{\theta}_3} \\ \frac{\partial\dot{z}}{\partial\dot{\theta}_1} & \frac{\partial\dot{z}}{\partial\dot{\theta}_2} & \frac{\partial\dot{z}}{\partial\dot{\theta}_3} \\ \frac{\partial\dot{\gamma}}{\partial\dot{\theta}_1} & \frac{\partial\dot{\gamma}}{\partial\dot{\theta}_2} & \frac{\partial\dot{\gamma}}{\partial\dot{\theta}_3} \end{bmatrix} = \begin{bmatrix} -1/3 & -1/3 & -1/3 \\ -l\sin\theta_1/3 & -l\sin\theta_2/3 & -l\sin\theta_3/3 \\ -l\theta_1/2d & 0 & l\theta_3/2d \end{bmatrix} \tag{29}$$

$$\tau = J^T F = \begin{bmatrix} -1/3 & -l\sin\theta_1/3 & -l\theta_1/2d \\ -1/3 & -l\sin\theta_2/3 & 0 \\ -1/3 & -l\sin\theta_3/3 & l\theta_3/2d \end{bmatrix} \begin{bmatrix} F_y \\ F_z \\ N_\gamma \end{bmatrix} \tag{30}$$

Since we are interested in just the effect on pitch, we consider only the last column of the J^T relationship:

$$\tau_1 = \frac{-1\theta_1}{2d} N_\gamma \qquad (31)$$
$$\tau_2 = 0$$
$$\tau_3 = \frac{1\theta_3}{2d} N_\tau$$

This relationship relates the hip torques applied at the front and rear hips to their contribution to the moment about the centre of mass.

Normally, these equations are applied to manipulators in which a single link is grounded, so that torques applied in actuators are balanced by constraint forces at the manipulator's grounded link. However, in this case the 'base link' is the robot's body, and we are interested in torques applied about its pitch axis. The torque seen about the pitch axis of the robot will equal the sum of the kinematic contribution and the contribution due to Newton's third law for torques, translated (by means of the parallel axis theorem [48]) according to their effect on the angular acceleration about the center of mass:

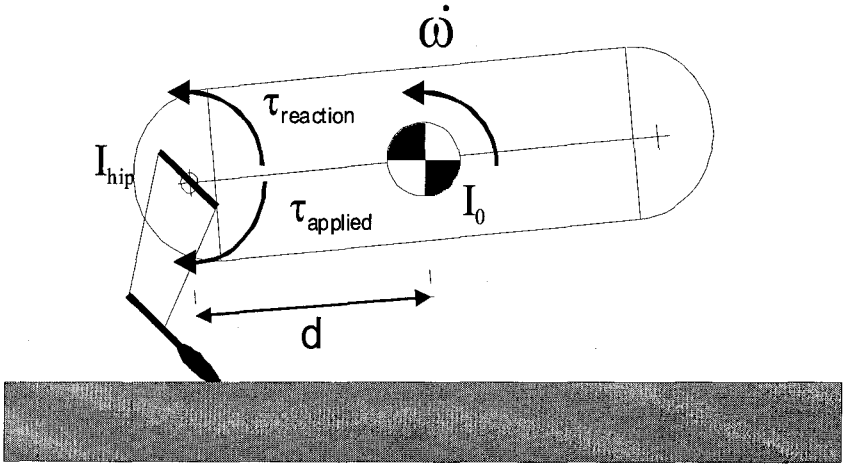

Figure 50: Effect of applied hip torques on the angular acceleration about the center of mass

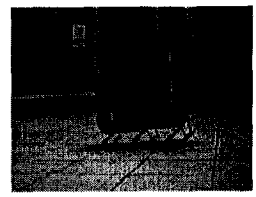

$$
\begin{aligned}
I_a\dot{\omega} &= \tau_{reaction} \\
\left(I_0 + md^2\right)\dot{\omega} &= \tau_{reaction} \\
N_{ntnIII} &= I_0\dot{\omega} \\
N_{ntnIII} &= \frac{\tau_{reaction}}{\left(I_0 + md^2\right)} I_0 \\
N_{ntnIII} &\cong \frac{\tau_{reaction}}{\left(0.1 + 7.6kg(0.2m)^2\right)} 0.1 \\
N_{ntnIII} &\cong 0.247\tau_{reaction}
\end{aligned}
\tag{32}
$$

This approximation finally allows the computation of the relationship between front and rear hip torques and the pitch moment generated about the center of mass.

$$
\begin{aligned}
N &= N_{ntnIII} + N_{J^T\tau_1} \\
N &= -\left(\frac{2d}{1\theta_1} + 0.247\right)\tau_1 + \left(\frac{2d}{1\theta_3} - 0.247\right)\tau_3 \\
\tau_1 &\propto \frac{N}{-\left(\frac{2d}{1\theta_1} + 0.247\right)} \quad \tau_3 \propto \frac{N}{\left(\frac{2d}{1\theta_3} - 0.247\right)}
\end{aligned}
\tag{33}
$$

In theory, this relationship should allow us to command a 'virtual' torque of N Nm about the centre of mass. Assuming N gives rise to torques τ_1, τ_2 within the motor saturation limits, we should then observe an angular acceleration of N/I_0 greater than the angular acceleration when no pitch moment is applied.

Touchdown plane control

Another crucial interaction that may affect robot pitch is the non-simultaneous touchdown of each of the robot's six legs. In this section, a method to exploit this for the benefit of pitch control is explored experimentally.

Though the equations of motion governing the motion of the robot during a general multi-legged touchdown will not be the subject of this work, it is hoped that useful and insightful relationships between the order of leg touchdown and the effect on robot pitch may be obtained through a hypothesis-based empirical approach.

To this end we hypothesise that early touchdown of either the front or rear legs provides a pivot point about which a torque will be generated by the falling motion of the robot. We test this hypothesis by constraining the robot's toes to a plane with a controllable angle with respect to the horizontal plane.

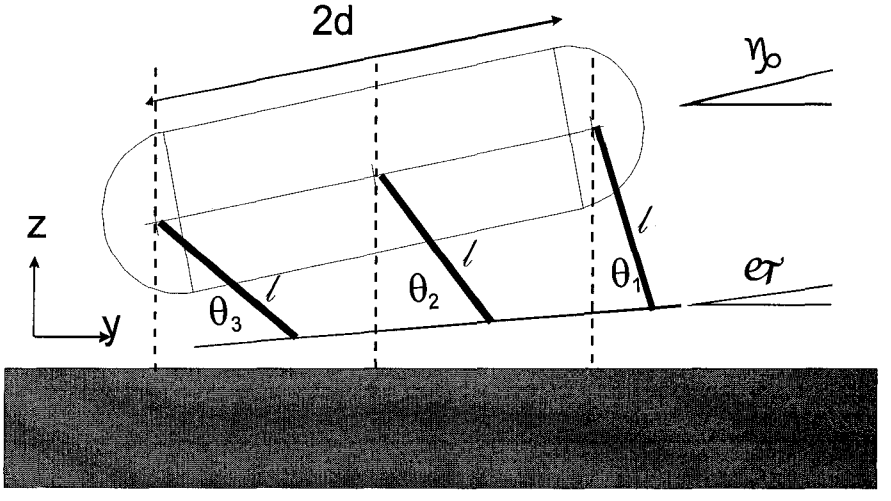

Figure 51: Constraining the toes to a touchdown plane

To calculate the required hip angles, the middle leg hip angle is first selected to allow control of the angle of the touchdown plane. Then the front and rear angles are calculated. The height of each hip with respect to the toe plane is approximated as $l\cos(\theta)$.

$$
\begin{aligned}
&\text{- choose } \theta_1 && \sin\varphi = \frac{l(\cos\theta_1 - \cos\theta_3)}{2d} \\
&\cos\theta_2 = \cos\theta_1 - \frac{d\sin\varphi}{l} && \sin\varphi = \frac{l(\cos\theta_1 - \cos\theta_2)}{d} \\
&\cos\theta_3 = \cos\theta_1 - \frac{2d\sin\varphi}{l} && \sin\varphi = \frac{l(\cos\theta_2 - \cos\theta_3)}{d}
\end{aligned}
\qquad (34)
$$

Constraining the toes to a particular plane is not strictly required, it simply allows continuously variable one-parameter control over the touchdown order.

So far consideration is only being given to the touchdown order of the toes. However, strong dynamical effects may be caused by the leg postures resulting from adherence to the touchdown plane constraint. We do not attempt to explain these yet—we will first see if variation of the touchdown plane parameter has a strong or weak control over the robot's pitch at touchdown and during stance.

5.4 Experimental validation

Kinematic Pitch Control

To test the above hypotheses, a system was devised for dropping the robot from a fixed height at close to zero pitch and pitch rate. The onboard gyroscope (see section "An Attitude Estimator for RHex") and software attitude integrator were used to measure the pitch rate and pitch respectively.

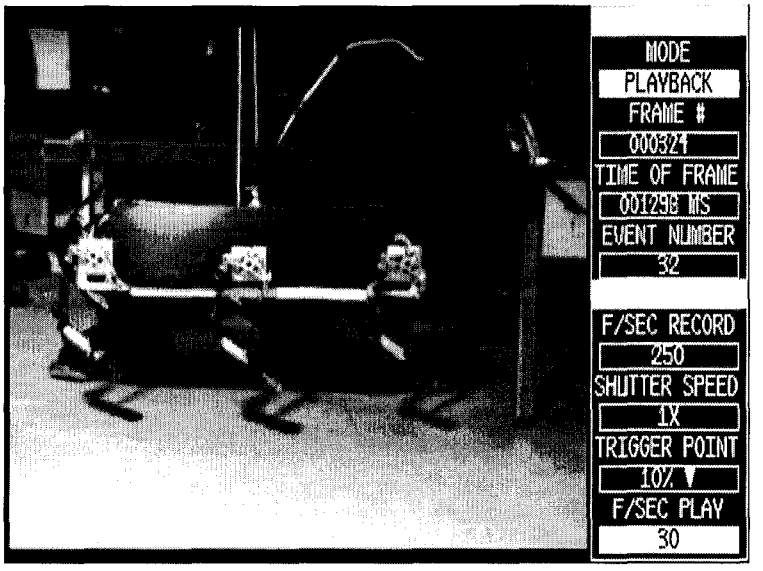

Figure 52: Drop test experimental setup

For each experiment the robot was held against a levelling bar, then allowed to drop, bouncing off the ground and flying for a short time before being caught by the attached wrangle.

For the kinematic pitch control experiments, commands of ±100 Nm and zero Nm (for comparison) were requested at a nominal touchdown angle of 10°.

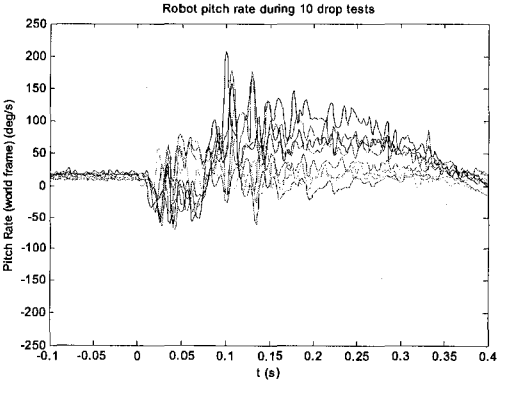

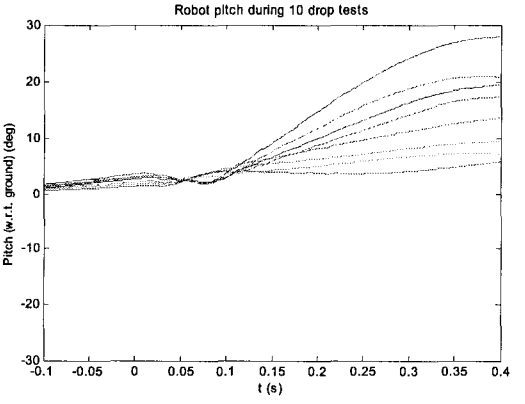

Figure 53a,b: Robot pitch and pitch rate for +100 Nm command

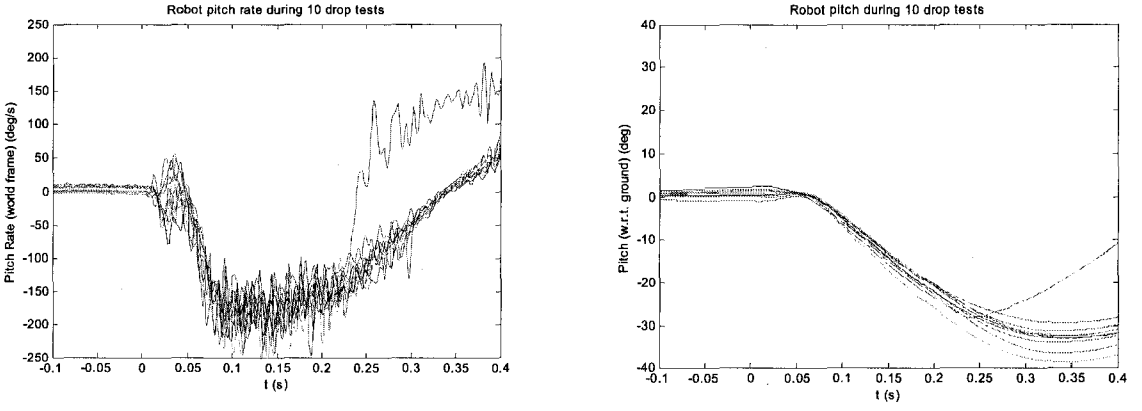

Figure 54a,b: Robot pitch and pitch rate for -100 Nm command

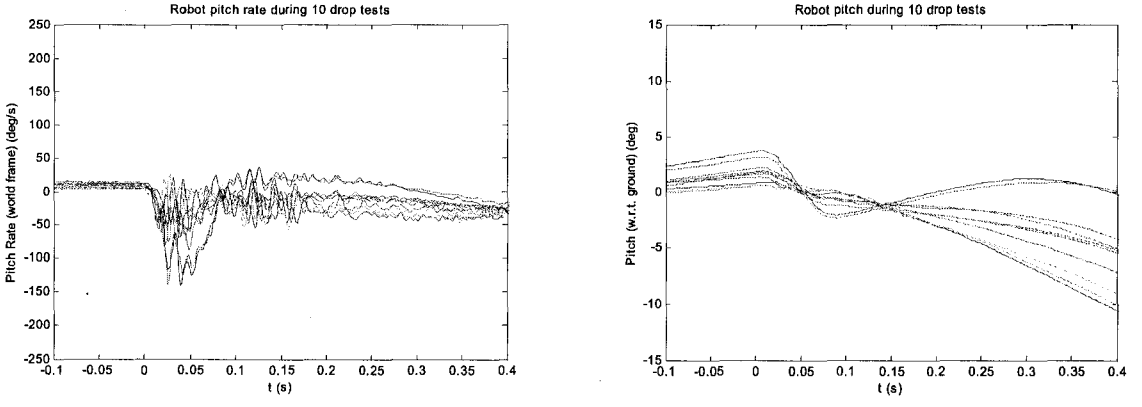

Figure 55a,b: Robot pitch and pitch rate for 0 Nm command

Touchdown Plane Control

Similar results were obtained for drop tests with touchdown plane control. In this case, middle legs were set for 15° touchdown angle, and the requested touchdown plane angles were ±2 degrees and zero. Figures Figure 56, Figure 57 and Figure 58 show the effect of touchdown plane variation on body pitch after impact.

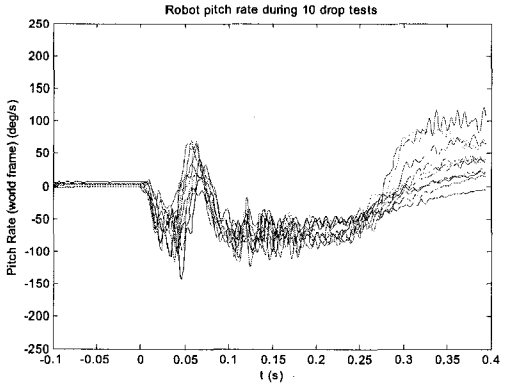

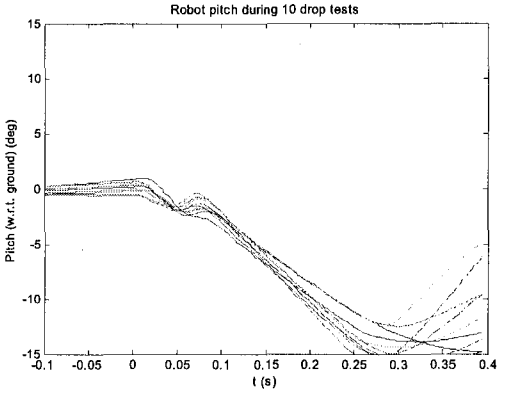

Figure 56a,b: Robot pitch and pitch rate for +2° touchdown plane angle

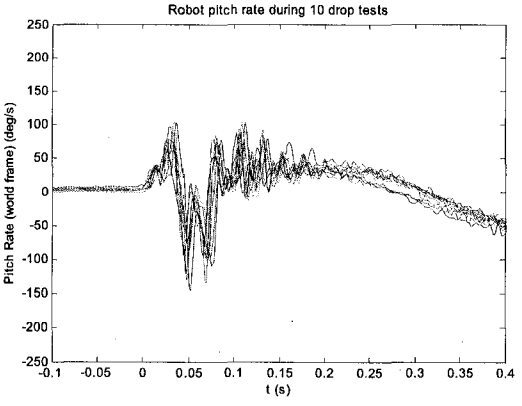

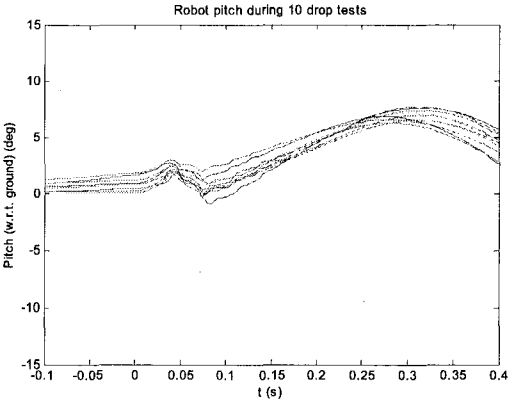

Figure 57a,b: Robot pitch, pitch rate for -2° touchdown plane angle

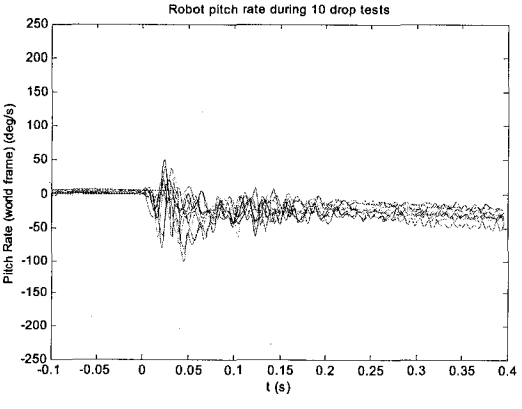

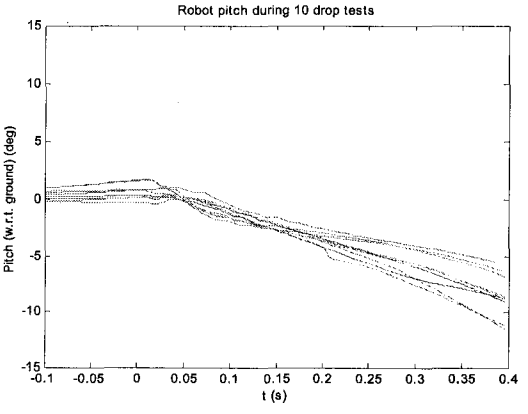

Figure 58a,b: Robot pitch and pitch rate for 0° touchdown plane angle

5.5 Discussion

Both methods described above show substantial control over robot pitch. However, for kinematic pitch control the control relationship seems to be stronger for negative commands than for positive ones, possibly due to the robot's posture (+10° touchdown angle for all legs).

Unfortunately, while these methods resulted in control over pitch during drop test experiments, they disrupted the motion of the robot so much that neither method could be used successfully to control pitch during pronking. Touchdown plane control appeared to disturb the robot's touchdown angles enough to cause skidding. Kinematic pitch control disrupted the backward motion of the legs during stance with forward torques.

Chapter 6 Conclusion and Future Work

This thesis presented the development of an open-loop pronking gait for RHex. This gait demonstrated the fact that fast, efficient locomotory behavior may be derived from very simple control algorithms when the robot is appropriately designed. A basic model of how pronking works in RHex was presented and validated both in simulation and experiment. RHex was able to pronk successfully for relatively long durations over flat surfaces. However, the open-loop pronking gait did not demonstrate robustness to changes in surface material, control parameters, or even battery state-of-charge. From these developments, the following conclusions may be drawn:

- Complex and useful locomotory behavior can be achieved with rudimentary control and appropriate mechanical design.
- Stability in the case of open-loop controllers depends on the passive dynamic behavior of the system.
- With pronking, the passive dynamic behavior appeared to be marginally stable.
- More sophisticated control was therefore required to render pronking stable.

The lack of robustness exhibited by the open-loop pronk led the author to examine the possibility of a more active control of balance during pronking through a succession of experiments designed to control the pitch of the robot at takeoff. Though control of robot pitch was demonstrated, the author was unable to control pitch using these methods while pronking, primarily due to their interference with the normal motion of the legs during pronking.

Future work in running gaits on RHex will very likely focus on exploiting the same springy legged dynamics discussed in this thesis and other the writings of many colleagues. Though the attitude estimation system described provides excellent orientation information, augmenting it with a forward speed sensor (either a "virtual sensor" based on kinematics during stance or an external velocity sensor) would allow the implementation of Raibert's foot placement algorithm. Full implementation of this algorithm might be the first step in improving the stability of pronking and other running gaits.

The addition of a second (thrusting) actuator to RHex's compliant four-bar legs (the legs used for pronking) could allow the addition of energy to the gait without disrupting the stance phase dynamics. This would not only make the gait easier to stabilize, but would also allow more direct control over hopping height. Actuation for a radial degree of freedom is already under development, and may result in the ability to thrust during stance in the near to medium term.

Appendix A: MB v 1.3 Motor Driver Board Design Documents

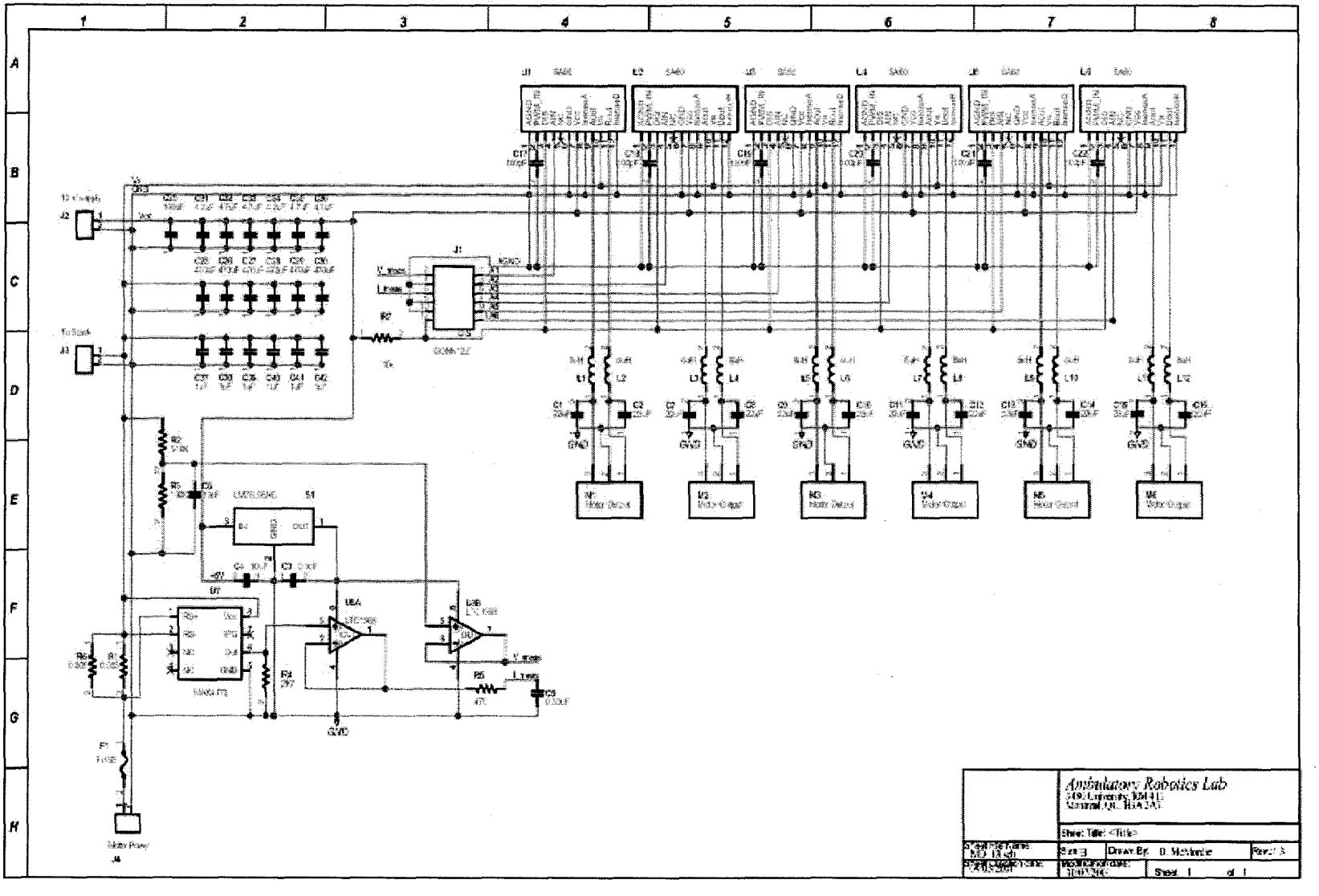

Top Layer

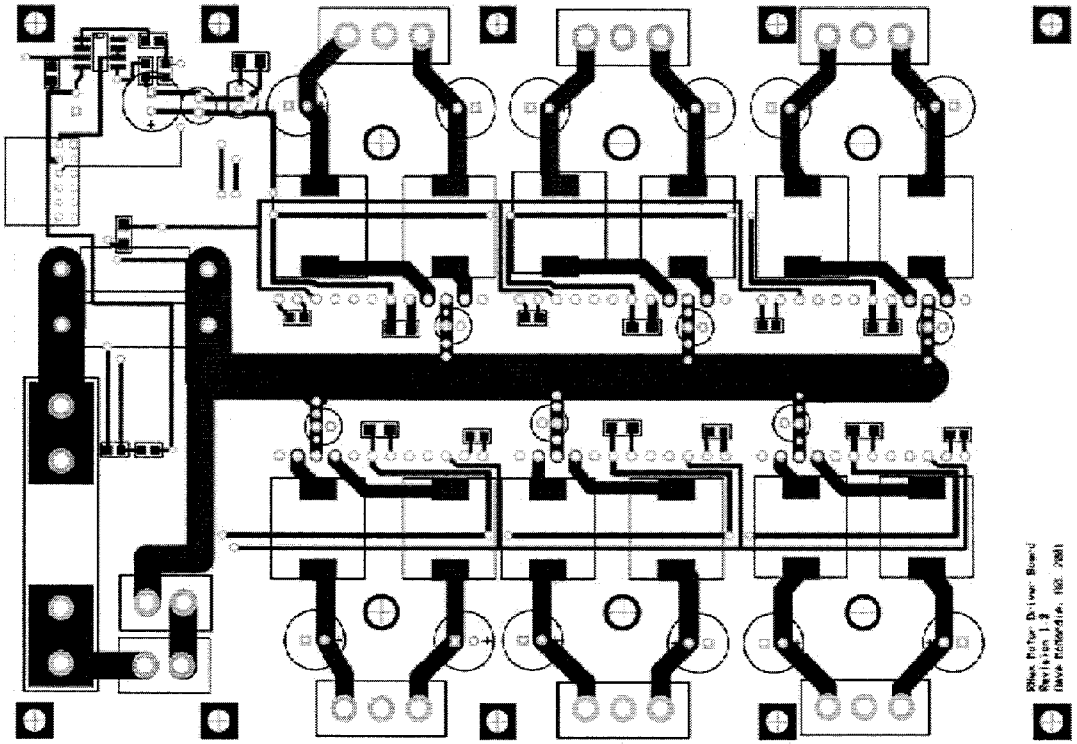

Bottom Layer

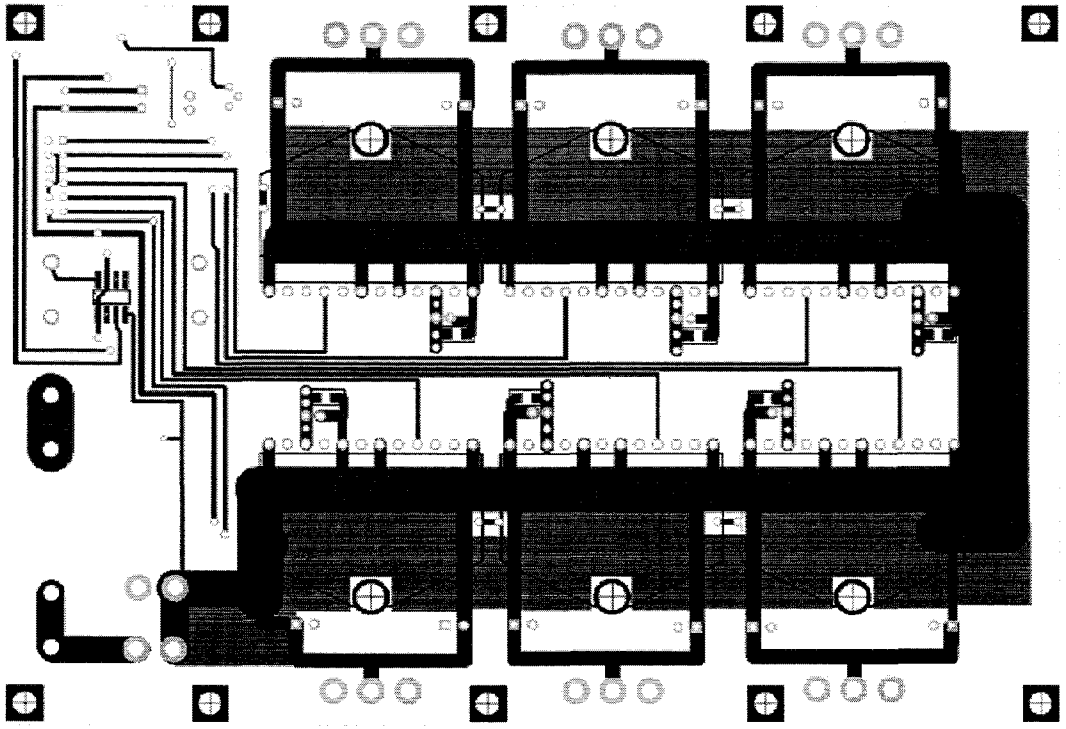

Heat sink

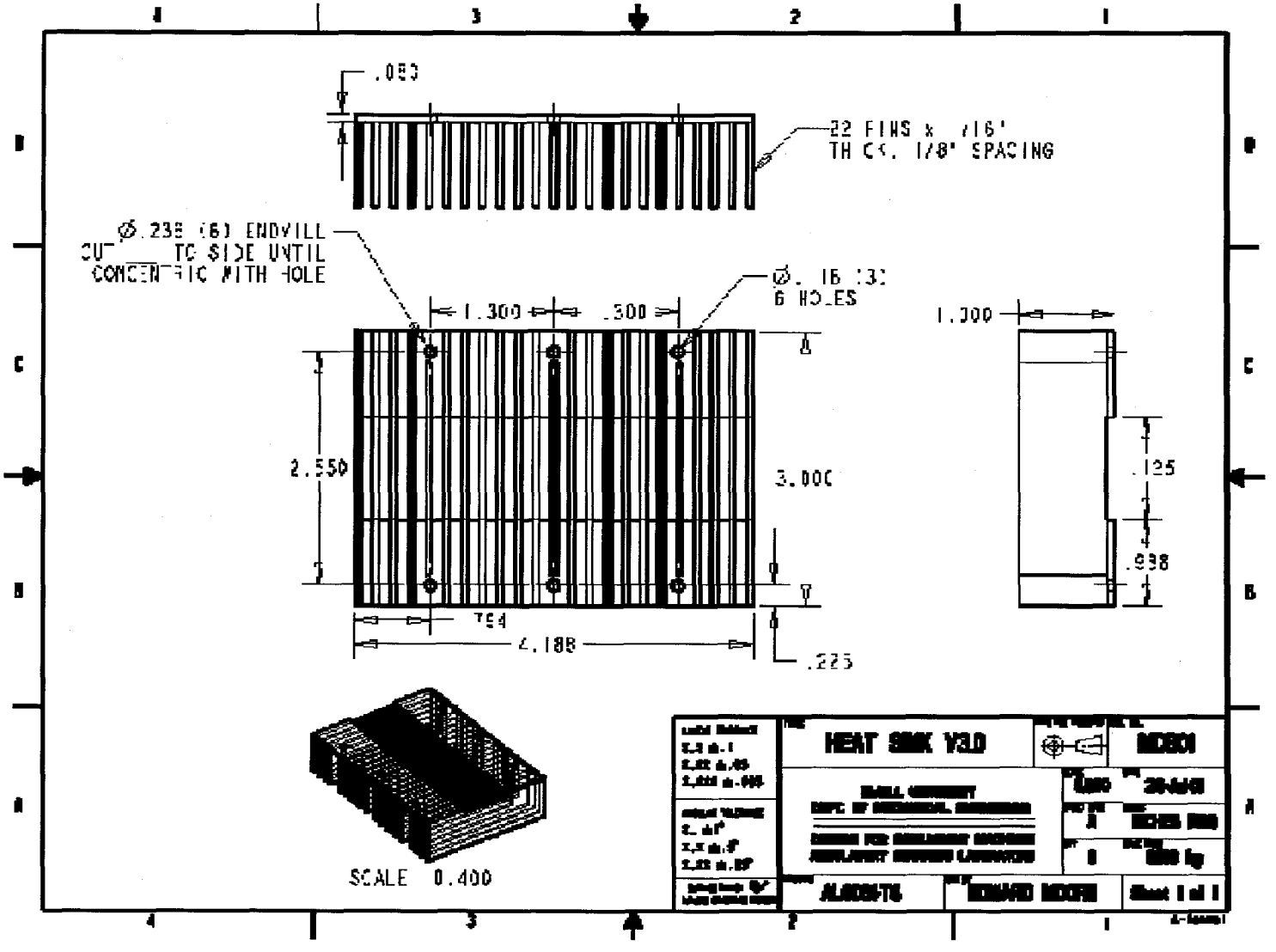
.050
22 FINS x .716'
TH CK. 1/8" SPACING
Ø.238 (6) ENDVILL
CUT TO SIDE UNTIL
CONCENTRIC WITH HOLE
Ø.116 (3)
6 HOLES
1.300
.300
1.300
2.550
3.000
.125
.938
TS4
4.188
.225
SCALE 0.400
HEAT SINK V3.0

VG941-3D gyroscope interface-- schematic

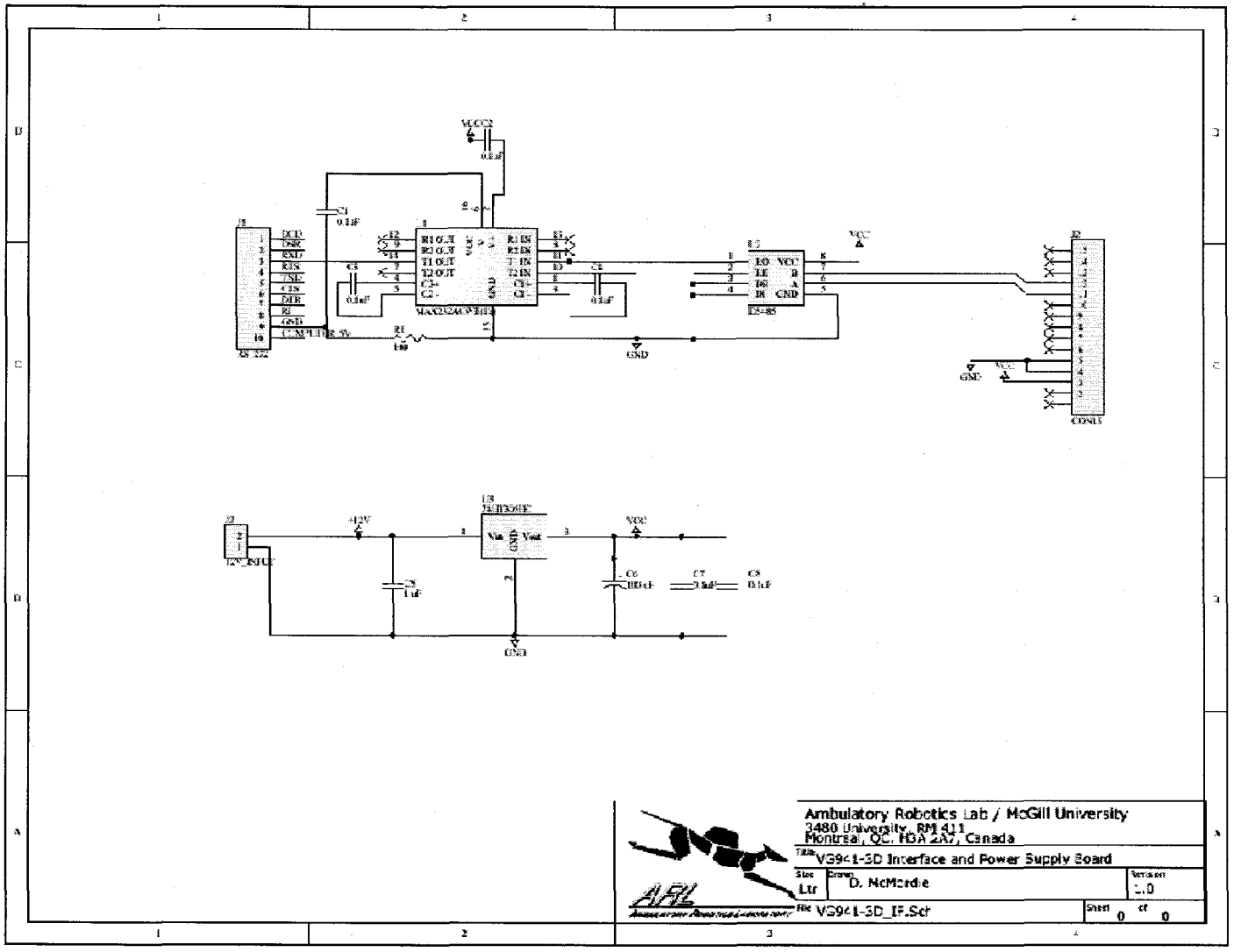

VG941-3D gyroscope interface-- board layout

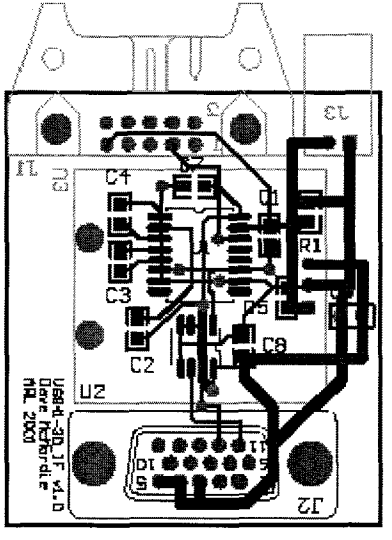

Bibliography

[1] iRobot Corp., Twin City Office Center, 22 McGrath Highway, Suite 6, Somerville, MA 02143. www.irobot.com

[2] Dickinson, M.H., et al.. "How Animals Move: An Integrative View". *Science*, 288, 100-106. April, 2000

[3] U. Saranli, M. Buehler, D.E. Koditschek, "RHex: A Simple and Highly Mobile Hexapod Robot", *Int. J. Robotics Research*, 20(7):616-631, July 2001

[4] Kubow, T.T. and Full, R.J. "The role of the mechanical system in control: a hypothesis of self-stabilization in hexapedal runners", *Phil. Trans. R. Soc. Lond.* B. (1999) 354, 849-861.

[5] Nutan Shukla, "Yo-yos of the animal kingdom", article in The Tribune Online Edition, Chandigarh, India. Viewed online at: http://www.tribuneindia.com/2002/20020331/spectrum/nature.htm

[6] M. Raibert, "Hopping in Legged Systems—Modeling and Simulation for the Two-Dimensional One-Legged Case". *IEEE Trans. Systems, Man, and Cybernetics*, 14 (3):451–463, May/June 1984.

[7] M. Raibert, M. Chepponis and H. B. Brown, "Running on Four Legs As Though They Were One", *IEEE J. Robotics and Automation*, 2(2): 70-82, June 1986.

[8] Seyfarth, A., Geyer H., Guenther, M. and Blickhan, R., "A Movement Criterion for Running", *J. Biomechanics*, vol 35, 649-655, 2002.

[9] M. Ahmadi and M. Buehler, "Stable Control of a Simulated One-Legged Running Robot with Hip and Leg Compliance". *Proc. IEEE Transactions on Robotics and Automation*, 13(1):96-104, Feb 1997.

[10] M. Buehler, A. Cocosco, K. Yamazaki, and R. Battaglia, "Stable Open Loop Walking in Quadruped Robots with Stick Legs," *Proc. IEEE Int. Conf. Robotics and Automation*, p. 2348-2353, Detroit, Michigan, May 1999.

[11] M. de Lasa and M. Buehler, "Dynamic Compliant Quadruped Walking", *Proc. IEEE Int. Conf. on Robotics and Automation*, pp 3153-3158, Seoul, Korea, May, 2001.

[12] R. A. Brooks, "A robot that walks; emergent behaviors from a carefully evolved network" *Proc. IEEE Int. Conf. on Robotics and Automation*, 1989. 14-19 May 1989 Page(s): 692 -4+2 vol.2

[13] J. Clark *et al.*, "Biomimetic Design and Fabrication of a Hexapedal Running Robot", *Proc. IEEE Int. Conf. on Robotics and Automation,* Seoul, Korea, May 2001.

[14] M. D. Berkemeier, "A Model for Quadruped Running-in-place in the Plane". *Proc. 35th IEEE Int. Conf. on Decision and Control*, Kobe, Japan, 1996

[15] M. Raibert, M. Chepponis and H. B. Brown, "Running on Four Legs As Though They Were One". *IEEE J. Robotics and Automation*, 2(2): 70-82, June 1986.

[16] S. Talebi, I. Poulakakis, E. Papadopoulos, and M. Buehler, "Quadruped Robot Running with a Bounding Gait", *Int. Symp. Experimental Robotics*, Honolulu, HI, Dec 2000.

[17] Micro Switch Inc. (a Honeywell division) "Installation instructions for CS series adjustable linear current sensors", document PK 8790 1.

[18] Micro/sys Inc., "Analog, Digital and Timer I/O for PC/104 MPC550", http://www.embeddedsys.com/subpages/products/images/pdf/microsys_mpc550_datasheet.pdf

[19] Apex Microtechology, "SA60 Datasheet" (www.apexmicrotech.com) SA60U Rev. F

[20] Apex Microtechnology, "PWM Low Pass Filtering". Application note 32. (www.apexmicrotech.com)

[21] J. W. Miller Inc., "High Current Toroid Inductors" (catalog page 126) http://www.jwmiller.com/pdf2/6700.pdf

[22] E. Moore, *Leg Design and Stair Climbing Control for the RHex Robotic Hexapod*, M. Eng. Thesis, McGill University, 2001.

[23] Obaid, Sami Y., "Sensing for Dynamic Locomotion". M. Eng. Thesis, McGill University, August, 1999.

[24] Litton Guidance and Control Systems, "Litton G2000 Gyroscope", document number GCS 22195 3/99.

[25] Lefèvre, Hervé, "Fundamentals of the interferometric fiber optic gyroscope", Proc. SPIE Vol. 2837, 2-17, Nov, 1996.

[26] S. Bennett, S. Emge and R. Dyott, "Fiber Optic Gyros for Robotics". Viewed online at: http://www.kvh.com/pdf/fog_robots.pdf.

[27] Sagnac, G., "L'ether lumineux demontre par l'effet du vent relatif d'ether dans un interferometre en rotation uniforme", *Comptes Rendues d'Academie de Science Français.* Vol. 95 pp. 708-719, 1913.

[28] S. M. Bennett, et al., "Fiber optic rate gyros as Replacements for Mechanical Gyros". AIAA Guidance, Navigation, and Control Conference and Exhibit, Boston, MA, Aug. 10-12, 1998 (viewed online at: http://www.kvh.com/pdf/aiaa98.pdf)

[29] Ojeda, L., Chung, H. Borenstein, J., "Precision-calibration of Fiber-optics Gyroscopes for Mobile Robot Navigation", Proc. 2000 IEEE Conf. Robotics and Automation, San Francisco, CA, April 24-28, 2000, pp 2064-2069.
[30] Murata MFG. CO. LTD., "Gyrostar® Piezoelectric Vibrating Gyroscope ENC Series", catalog S42E-2, 1999.
[31] Murata MFG. CO. LTD., "Operation Manual of Gyrostar™ Piezoelectric vibrating Gyroscope Model: ENV-05F-3 Support sensor for car navigation systems", Product Engineering Section, Sensor Module Department, Circuit Module Products Division, No. APENVF01E.
[32] KVH Technologies Inc., "KVH ECore 2000 Series Precision Fiber Optic Gyros" (brochure) viewed online at http://www.kvh.com/pdf/Ecore2000_1.02.pdf
[33] http://www.fizoptika.ru/products/catalog/vg941-3d.htm
[34] Farrell, J., *Integrated Aircraft Navigation*, Academic Press, New York, NY (1976), p 44
[35] Angles, J., *Fundamentals of Robotic Mechanical Systems*, New York: Springer, 1997. p 46, 93
[36] D. Wilkins, "Hamilton's Research on Quaternions". viewed online at: http://www.maths.tcd.ie/pub/HistMath/People/Hamilton/Quaternions.html
[37] "Sagnac Effect" http://www.mathpages.com/rr/s2-07/2-07.htm
[38] Fizoptika VG941 Manual
[39] Ojeda, L. Chung, H., Borenstein, J, "Precision Calibration of Fiber-optics Gyroscopes for Mobile Robot Navigation", Proc. 2000 IEEE Conf. Robotics and Automation, San Francisco, CA, April 24-28 2000, pp 2064-2069
[40] Parker Hannifin Corporation, "200RT Series" Catalog 8080 USA, page A53.
[41] M. Raibert, "Hopping in Legged Systems—Modeling and Simulation for the Two-Dimensional One-Legged Case". IEEE Trans. Systems, Man, and Cybernetics, 14(3):451–463, May/June 1984.
[42] D. McMordie and M. Buehler, "Towards Pronking with a Hexapod Robot", *4th Int. Conf. on Climbing and Walking Robots*, Karlsruhe, Germany, September 24 - 26 , 2001.
[43] H. Komsuoglu, D. McMordie, U. Saranli, N. Moore, M. Buehler, D. E. Koditschek, "Proprioception Based Behavioral Advances in Hexapod Robot", Proc. *IEEE Int. Conf. on Robotics and Automation*, pp 3650 - 3655, Seoul, Korea, May 21-26, 2001

[44] S. Hirose "A Study of Design and Control of a Quadruped Walking Vehicle", *Int. J. Robotics Research*, Vol 3, No 2, Summer 1984

[45] J. Koechling "Gait as Mechanical Oscillation", chapter in *Dynamically Stable Legged Locomotion*, Robotics Institute Technical Report CMU-LL-4-1985, Carnegie Mellon University, Pittsburgh

[46] J. Pratt, *Exploiting Inherent Robustness and Natural Dynamics in the Control of Bipedal Walking Robots*, Ph. D. Thesis, Massachusetts Institute of Technology, June, 2000

[47] Raibert, M., Chepponis, M., Brown, H. B., "Running on Four Legs As Though They Were One". *IEEE J. Robotics and Automation*, vol. RA-2, No. 2, June 1986.

[48] See Kleppner, D., Kolenkow, R., *An Introduction to Mechanics*, p 252. New York: McGraw-Hill Inc., 1973